The Role of Midlatitude Cyclones in the Emission, Transport, Production, and Removal of Aerosols in the Northern Hemisphere

Joseph Robinson[1], Lyatt Jaegle[1], and Luke D. Oman[2]

[1]University of Washington
[2]NASA Goddard Space Flight Center

December 7, 2022

Abstract

We examine the distribution of aerosol optical depth (AOD) across 27,707 northern hemisphere (NH) midlatitude cyclones for 2005-2018 using retrievals from the Moderate Resolution Spectroradiometer (MODIS) sensor on the Aqua satellite. Cyclone-centered composites show AOD enhancements of 20-45% relative to background conditions in the warm conveyor belt (WCB) airstream. Fine mode AOD (fAOD) accounts for 68% of this enhancement annually. Relative to background conditions, coarse mode AOD (cAOD) is enhanced by more than a factor of two near the center of the composite cyclone, co-located with high surface wind speeds. Within the WCB, MODIS AOD maximizes in spring, with a secondary maximum in summer. Cyclone-centered composites of AOD from the Modern Era Retrospective analysis for Research and Applications, version 2 Global Modeling Initiative (M2GMI) simulation reproduce the magnitude and seasonality of the MODIS AOD composites and enhancements. M2GMI simulations show that the AOD enhancement in the WCB is dominated by sulfate (37%) and organic aerosol (25%), with dust and sea salt each accounting for 15%. MODIS and M2GMI AOD are 60% larger in North Pacific WCBs compared to North Atlantic WCBs and show a strong relationship with anthropogenic pollution. We infer that NH midlatitude cyclones account for 355 Tg yr^{-1} of sea salt aerosol emissions annually, or 60% of the 30-80^{o}N total. We find that deposition within WCBs is responsible for up to 35% of the total aerosol deposition over the NH ocean basins. Furthermore, the cloudy environment of WCBs leads to efficient secondary sulfate production.

The Role of Midlatitude Cyclones in the Emission, Transport, Production, and Removal of Aerosols in the Northern Hemisphere

Joseph Robinson[1], Lyatt Jaeglé[1], Luke D. Oman[2]

[1]Department of Atmospheric Sciences, University of Washington, Seattle, WA, USA

[2]Atmospheric Chemistry and Dynamics Laboratory, NASA Goddard Space Flight Center, Greenbelt, MD, USA

Corresponding author: Joseph Robinson (jrobin15@uw.edu)

Key Points:

- Satellite observations show 20-45% enhancement of aerosol optical depth (AOD) in the warm conveyor belt airstream of midlatitude cyclones
- A global model attributes 37% of these enhancements to sulfate, 25% to organic carbon, 15% to dust, and 15% to sea salt aerosol
- Midlatitude cyclones lead to 355 Tg yr^{-1} of sea salt aerosol emissions, or 60% of the total over the northern hemisphere oceans

Abstract

We examine the distribution of aerosol optical depth (AOD) across 27,707 northern hemisphere (NH) midlatitude cyclones for 2005-2018 using retrievals from the Moderate Resolution Spectroradiometer (MODIS) sensor on the Aqua satellite. Cyclone-centered composites show AOD enhancements of 20-45% relative to background conditions in the warm conveyor belt (WCB) airstream. Fine mode AOD (fAOD) accounts for 68% of this enhancement annually. Relative to background conditions, coarse mode AOD (cAOD) is enhanced by more than a factor of two near the center of the composite cyclone, co-located with high surface wind speeds. Within the WCB, MODIS AOD maximizes in spring, with a secondary maximum in summer. Cyclone-centered composites of AOD from the Modern Era Retrospective analysis for Research and Applications, version 2 Global Modeling Initiative (M2GMI) simulation reproduce the magnitude and seasonality of the MODIS AOD composites and enhancements. M2GMI simulations show that the AOD enhancement in the WCB is dominated by sulfate (37%) and organic aerosol (25%), with dust and sea salt each accounting for 15%. MODIS and M2GMI AOD are 60% larger in North Pacific WCBs compared to North Atlantic WCBs and show a strong relationship with anthropogenic pollution. We infer that NH midlatitude cyclones account for 355 Tg yr^{-1} of sea salt aerosol emissions annually, or 60% of the 30-80^{o}N total. We find that deposition within WCBs is responsible for up to 35% of the total aerosol deposition over the NH ocean basins. Furthermore, the cloudy environment of WCBs leads to efficient secondary sulfate production.

Plain Language Summary

Largescale storms occur during all seasons in the northern hemisphere midlatitudes and are responsible for a significant fraction of observed midlatitude precipitation. The meteorological environment of these cyclones influences the direct emission, removal, chemistry, and transport of aerosols. This study combines satellite observations and a global computer simulation to probe each of these processes. To do so, cyclone-centered composites are generated by averaging together 27,707 individual northern hemisphere cyclone cases between 2005-2018. Results show that the total column amount of aerosol within the rain-producing part of cyclones is enhanced and that most of this enhancement is in the form of smaller aerosol particles more likely associated with human activities. Cyclone region and season play a large role in the abundance of aerosol, with springtime cyclones downwind of Asia displaying the largest abundances. We find that strong winds within cyclones account for over half of the annual direct emission of sea salt aerosol over the northern hemisphere oceans. Furthermore, we show that midlatitude cyclones efficiently remove aerosol, accounting for 27-33% of the total over the northern hemisphere ocean basins. They also account for 27% of secondary production of sulfate and facilitate aerosol transport.

1 Introduction

Tropospheric aerosols exert considerable influence on earth's climate, ecosystems, and human health. Aerosols substantially perturb Earth's radiation balance both directly by scattering and absorbing solar radiation and indirectly by altering cloud properties (Myhre et al., 2013; Partanen et al., 2018; Shindell et al., 2013; Smith & Bond, 2014; Westervelt et al., 2015). Nutrients in the form of iron and nitrate aerosols are transported from land and deposited into ocean environments where they can promote primary production (Baker et al., 2003; Jickells &

Spokes, 2001). Exposure to increased levels of fine particulate matter has also been shown to result in as many as 4.2 million premature deaths each year globally (Fang et al., 2013; Silva et al., 2017).

Explaining the full spectrum of aerosol emissions, aerosol secondary formation via oxidation of precursor gases, transport, and removal pathways has therefore been the subject of continual research in recent decades (Alfaro & Gomes, 2001; Andreae & Crutzen, 1997; Graedel & Weschler, 1981; Jacobson & Hansson, 2000; Kerminen et al., 2005; Prather, et al., 2008). Despite these efforts, large uncertainties remain in our understanding of these aerosol processes and their representation in models (Guibert et al., 2005; Hodzic et al., 2016; Kinne et al., 2003; Real et al., 2010; Q. Yang et al., 2015).

Midlatitude cyclones are at the intersection of processes controlling the regional and global distribution of tropospheric aerosols. The ability of their warm conveyor belts (WCBs) to lift air masses into the free troposphere and redistribute them globally is a dominant pathway for the export of pollution from Asia and North America (Hannan et al., 2003; Jaffe et al., 2003; Liang et al., 2004; Sinclair et al., 2008). Research in recent decades has tried to better characterize the timing and extent of this export as well as its impact on downwind regions (e.g., Ding et al., 2009; Eguchi et al., 2009; Luan & Jaeglé, 2013; Y. Yang et al., 2015; Yu et al., 2008). For example, Yu et al. (2008) used monthly satellite observations of aerosol optical depth (AOD) during a 4-year period to estimate 18 Tg of pollution aerosol is exported from the Asian continent each year. Luan & Jaeglé (2013) used daily satellite observations and a chemical transport model to examine aerosol transport off both Asia and North America, finding AOD to be enhanced by more than 50% during export events. Precipitation associated with midlatitude cyclones can act to remove soluble aerosols and their precursors (Park et al., 2005). Extensive cloud cover also provides a favorable environment for aerosol formation via aqueous sulfur dioxide (SO_2) oxidation and growth during subsequent transport (Brock et al., 2004; Dunlea et al., 2009). Lastly, strong surface winds within the cyclone can result in enhanced sea spray emissions over oceans (Grandey et al., 2011).

There has also been recent interest in quantifying the extent to which aerosols themselves influence midlatitude cyclones through their effects on clouds and precipitation (e.g., McCoy et al., 2018; Naud et al., 2017). McCoy et al. (2018) showed that aerosol-cloud interactions result in an increase in cloud liquid water content, overall cloud coverage, and albedo in midlatitude cyclones in both hemispheres. In addition, a strengthening of midlatitude cyclones in the North Pacific due to the increased abundance of aerosols over the pre-industrial period has either been predicted by modeling studies (Joos et al., 2017; Wang et al., 2014) or observed as increases in precipitation and the frequency of high clouds (Zhang et al., 2007). For example, Wang et al. (2014) used a multi-scale modeling approach to find precipitation is enhanced by 7-20% in North Pacific winter-time cyclones that occur under a predominantly polluted versus marine aerosol scenario.

Transport mediated by midlatitude cyclones occurs primarily along two coherent airstreams: the WCB and dry intrusion (DI). The WCB is the major ascending airstream of midlatitude cyclones (Browning & Roberts, 1994); it originates in the warm sector of the cyclone out ahead of the cold front and rapidly ascends moist isentropically from the boundary layer to the middle and upper troposphere as it travels poleward (Eckhardt et al., 2004; Stohl, 2001). Lifting of warm, moist air in the WCB results in widespread cloud cover and intense precipitation that culminates in a hallmark comma-shaped structure (Catto et al., 2010; Whitaker et al., 1988). In the upper troposphere, the WCB can turn anticyclonically in the stronger westerly flow or turn cyclonically and become aligned vertically with the surface low (Whitaker et al., 1988). Conversely, the DI originates in the upper troposphere or lower stratosphere and descends while fanning out behind the surface cold front. Downward transport of cold, dry air leads to little cloud cover and the presence of the “dry slot” as viewed on true color satellite imagery (Browning, 1997).

In the present study, our aim is to systematically examine the processes affecting AOD distributions within northern hemisphere (NH) midlatitude cyclones. The primary tool we use to accomplish this aim is cyclone-centered compositing across 27,707 midlatitude cyclones over a 14-year period (2005-2018). We composite these individual cyclones to analyze AOD as observed by the Moderate Resolution Imaging Spectroradiometer (MODIS) aboard the NASA Aqua satellite. We compare the resulting AOD composites to simulations from the NASA Modern Era Retrospective analysis for Research and Applications, version 2 Global Modeling Initiative (M2GMI) global chemistry climate model and use these simulations to interpret the observed structures in the AOD composites.

Grandey et al. (2011) generated midlatitude cyclone composites of satellite AOD and showed a strong positive relationship between AOD and surface wind speeds within the cyclone, consistent with wind-speed dependent emissions of sea salt aerosol (SSA). In a separate analysis, Grandey et al. (2013) found a positive relationship between cloud coverage and AOD in North Atlantic cyclones, but a negative relationship between AOD and cloud top temperature. They concluded that storm structure and strength could only explain a small fraction of these relationships and that aerosol-cloud interactions were likely part of the cause. Naud et al. (2016) examined the distribution of MODIS AOD using composites of midlatitude cyclones over the NH oceans. They also found a positive relationship between AOD and cloud cover in NH midlatitude cyclones and noted that the largest AOD values often occur along frontal boundaries within the cyclone domain where precipitating clouds form.

We build upon these previous studies by quantifying the extent to which the midlatitude cyclone environment induces aerosol vertical transport, scavenging, in-cloud oxidation of aerosol precursors, hygroscopic growth, emission of SSA, and ultimately results in aerosol export to the global atmosphere.

In section 2 we describe the observations and models used in our analysis. We present our cyclone identification methodology and compositing approach in section 3. In section 4 we analyze AOD composites obtained from MODIS observations and M2GMI simulations and examine the seasonal variation of AOD within cyclone WCBs. In section 5 we use vertical profiles of aerosol extinction from M2GMI to examine how enhancements vary throughout the troposphere. In section 6 we use M2GMI to quantify the contributions of midlatitude cyclones to SSA emissions and aerosol budgets over the NH oceans before summarizing in section 7.

2 Observations and Models

2.1 MODIS AOD Observations

We use AOD retrievals from the MODIS instrument onboard the NASA Aqua satellite (Remer et al., 2005). Aqua orbits at an altitude of 705 km with a 16 day repeat cycle and an equatorial crossing local time of 13:30. MODIS measures reflected solar radiation and emitted thermal radiation in 36 spectral channels, six of which are used to conduct aerosol retrievals (Levy et al., 2013; Remer et al., 2005, 2008). The 2,330 km swath of MODIS provides near daily global coverage. We use the combined quality controlled 550 nm AOD (dataset "Aerosol_Optical_Depth_Land_Ocean_Mean") from the collection 6.1 level 3 MODIS atmosphere daily global product (MxD08_D3; Levy et al., 2013; Wei et al., 2019a). These level 3 data are gridded $1^o \times 1^o$ AODs obtained from the level 2 instantaneous products (Platnick et al., 2015). The dataset is built from the combined ocean (best) and land (corrected) retrievals which only contains AOD for filtered retrievals over dark targets. In particular, it includes Dark Target (Levy et al., 2013) ocean retrievals having quality assurance ≥ 1 and Dark Target land retrievals having quality assurance equal to 3.

We also use MODIS fine mode AOD (fAOD), which is available only over oceans (dataset "Aerosol_Optical_Depth_Small_Ocean_Mean"). MODIS assumes nine tropospheric aerosol models with varying sizes (Levy et al., 2003). These include four fine modes (effective radii 0.10, 0.15, 0.20, and 0.25 μm), which together account for fAOD, and five coarse modes: three for sea salt (effective radii 1.00, 1.50, 2.00 μm) and two for mineral dust (effective radii 1.50 and 2.50 μm. We refer to the sum of the five coarse modes as coarse mode AOD (cAOD).

Prior to retrieving AOD, MODIS reflectances are cloud cleared at spatial resolution of 500 m. The cloud-free reflectances are averaged in 10 km × 10 km pixels if at least 10 out of 400 are available. Because of this, MODIS can retrieve AOD even if a 10 km scene is not entirely cloud free. Beginning with MODIS collection 6 this procedure uses an updated cloud masking routine to alleviate a known issue where AOD was a factor of two too large in scenes with cloud cover >80% (Remer et al., 2008). We conduct additional filtering of the MODIS AOD for any potential remaining cloud contamination by discarding $1^o \times 1^o$ grid cells with cloud fraction (CF) exceeding 50%. This results in the removal of ~60% of the global 1^o grid cells.

2.2 Reanalysis and Model Datasets

In order to identify midlatitude cyclone centers we use sea-level pressure (SLP) from the NASA Modern Era Retrospective analysis for Research and Applications, version 2 (MERRA-2; Gelaro et al., 2017). MERRA-2 is the latest NASA reanalysis and is improved over its predecessor, MERRA, as a result of updates to the atmospheric general circulation model (Molod et al., 2015) and observing system (McCarty et al., 2016). MERRA-2 has a horizontal resolution of 0.5^o latitude × 0.625^o longitude and 72 vertical levels extending from the surface to 0.01 hPa. The SLP field used to create the midlatitude cyclone database for this study comes from the MERRA-2 assimilated meteorology product (GMAO, 2015). We average the SLP from its original 3-hourly temporal resolution and use daily means.

The M2GMI simulation is a combination of the Goddard Earth Observing System (GEOS), version 5 general circulation model (Molod et al., 2015) and the Global Modeling

Initiative chemistry mechanism (Duncan et al., 2007; Strahan et al., 2007). It is constrained by MERRA-2 meteorology (winds, temperature, and pressure) through a replay technique (Orbe et al., 2017). M2GMI has the same resolution as MERRA-2 (0.5° × 0.625°, 72 vertical levels) and currently covers the period of 1980-2019. Fossil fuel and biofuel emissions in M2GMI come from the MACCity Inventory (Granier et al., 2011) until 2010 while more recent years are scaled up following Representative Concentration Pathways (RCP 8.5) emissions. Full descriptions of the M2GMI simulation are provided in Nielsen et al. (2017) and Strode et al. (2019). M2GMI also includes a suite of idealized tracers. In this work, we use the 25-day anthropogenic carbon monoxide tracer (hereafter $AnthroCO_{25d}$). $AnthroCO_{25d}$ has emissions corresponding to anthropogenic CO but undergoes decay at an idealized, fixed time of 25 days.

M2GMI is interactively coupled to the Goddard Chemistry and Aerosol Transport (GOCART) module for aerosols. GOCART simulates the major tropospheric aerosols of sulfate, black carbon, organic carbon (OC), dust, and SSA and was initially described by Chin et al. (2002) and Ginoux et al. (2001). Nitrate was added as described in Bian et al. (2017). A complete description of aerosol emissions and treatment in GOCART has more recently been given in Chin et al. (2009) and Colarco et al. (2010). SSA emissions have been modified from the original Gong (2003) formulation by re-calibration to surface friction velocity and inclusion of a sea-surface temperature dependence (Jaeglé et al., 2011) as described in Randles et al. (2017). There are five size bins for SSA corresponding to radii of 0.03-0.1, 0.1-0.5, 0.5-1.5, 1.5-5.0, and 5.0-10.0 μm. Dust emissions are a function of the surface characteristics and wind speed following Ginoux et al. (2001). Dust is also represented by five size bins corresponding to radii of 0.1-1.0, 1.0-1.8, 1.8-3.0, 3.0-6.0, and 6.0-10.0 μm. Sulfate and carbonaceous species have primary emissions from fossil fuel and biofuel combustion, biomass burning, as well as biogenic sources for OC. Sulfate is also produced by oxidation of SO_2 and dimethyl sulfide (DMS). Loss processes for each species include dry deposition, large-scale wet removal, and convective scavenging. We do note that while emissions in M2GMI are similar to those in the MERRA-2 aerosol reanalysis (Randles et al., 2017), M2GMI does not constrain total AOD through the assimilation of satellite AOD and thus serves as an independent dataset with which to probe aerosol export.

The original SSA emissions in M2GMI (8,934 Tg yr^{-1}, 2005-2018) are similar to those used in MERRA-2 (9,318 Tg yr^{-1}, 2000-2014; Randles et al., 2017), but more than a factor of 2 larger than the recent analysis of Bian et al. (2019) (4,015 Tg yr^{-1}) who used the NASA GEOS model with the GOCART module. The SSA GOCART emission scheme and meteorology are the same for these three simulations, however Bian et al. (2019) used a global scaling factor of 0.4, while MERRA-2 and M2GMI use a scaling factor of 0.875. Bian et al. (2019) showed good agreement of their simulations with comparisons to aircraft observations of aerosol mass concentrations as well as AOD from AERONET and MODIS. We thus scale SSA emissions, mass concentrations, and AOD in M2GMI by a factor of 0.46 (=0.4/0.875). The resulting SSA emissions are 4,060 Tg yr^{-1}, consistent with a number of the estimates reviewed in Weng et al. (2020). As aerosols are assumed to be externally mixed in GOCART, this scaling does not impact the other aerosol species simulated.

Aerosol optical properties in GOCART are from the Optical Properties of Aerosols and Clouds (OPAC; Hess, et al., 1998; Koepke et al., 1997). Dust is assumed to be non-hygroscopic while the other species undergo varying degrees of growth at higher relative humidity (see Figure 2 in Chin et al., 2002). The AOD is calculated as $\tau = \beta M_d$, where β is the mass extinction efficiency (in $m^2\ g^{-1}$) and M_d is the dry aerosol mass loading (in $g\ m^{-2}$). The mass extinction efficiency is a function of the aerosol refractive indices, size distribution, particle density, and relative humidity; it is assumed to be maximum at a relative humidity of 99%. Aerosol mass concentrations and AOD from GOCART simulations have been extensively validated against both ground-based and satellite observations (Chin et al., 2002, 2009, 2014; Colarco et al., 2010; Nowottnick et al., 2010).

To compare M2GMI against MODIS, the hourly M2GMI AOD and fAOD (sum of sulfate, organic carbon, black carbon as well SSA, dust, and nitrate with radii less than 1.0 μm) are linearly interpolated in time to 2pm local (i.e., near the Aqua equatorial crossing time). In addition, we sample daily-averaged aerosol properties from M2GMI. Finally, we sample daily-averaged meteorological fields from M2GMI in order to examine the WCB and broader midlatitude cyclone environment.

3 Compositing Methodology

Many recent analyses have utilized composites built from fields sampled in a cyclone-centered reference frame (e.g., Booth, et al., 2018; Field & Wood, 2007; Grandey et al., 2011, 2013; McCoy et al., 2018; Naud et al., 2017, 2019). Although compositing hides the variability on a cyclone-by-cyclone basis, averaging across many cases enables common patterns associated with cyclone airstreams to emerge. Midlatitude cyclone composites in turn make it possible to study meteorological and chemical signatures, and their spatiotemporal variability, in a more general framework. Further, it provides a framework for testing whether these signatures are accurately captured by global models. The composites of Knowland et al. (2015) highlighted that the WCB of strong NH midlatitude cyclones tends to enhance CO and deplete ozone (O_3) in the middle and upper troposphere as it redistributes air from near the surface. Jaeglé et al. (2017) used cyclone-centered composites to quantify the stratosphere-to-troposphere (STT) O_3 flux associated with midlatitude cyclones, finding that DIs account for 42% of the NH extratropical O_3 STT flux.

In this study, we use an approach that (1) identifies NH midlatitude cyclones; (2) samples satellite/model meteorological and aerosol fields on a 4,000 km × 4,000 km cyclone-centered grid; and (3) generates composites and examines anomalies relative to similarly sampled background conditions.

3.1 NH Midlatitude Cyclone Identification

We use the method described by Patoux et al. (2009) to identify NH midlatitude cyclone centers in the daily-averaged MERRA-2 SLP field. In brief, a cyclone center is identified if: (1) the grid cell is a true local pressure minimum; (2) the pressure is at least 1 hPa less than the pressure averaged over the surrounding grid cells up to ± 4 indices; (3) the Laplacian of pressure averaged over the same grid cells is at least 0.5×10^{-10} hPa m^{-2}. When two or more centers are identified within 2,000 km of each other, we only select the center with the lowest central SLP. Cyclone centers are also filtered for SLP ≤ 1,010 hPa to focus our analysis on mature cyclones most likely to have a coherent WCB airstream and therefore stronger transport. Our approach is conducted in a Eulerian framework and does not track the position of individual cyclones during their life cycle.

For the 2005-2018 period, we identify 27,707 midlatitude cyclones with centers between 30-80^{o} N. These midlatitude cyclones are relatively evenly distributed by season, with 29% of cyclones occurring in spring (March-April-May; MAM), 20% in summer (June-July-August; JJA), 25% in fall (September-October-November; SON), and 26% in winter (December-January-February; DJF). The spatial distribution of midlatitude cyclones shows high occurrence frequency in the North Atlantic and North Pacific storm tracks (Figure S1), consistent with previous studies (e.g., Hoskins & Hodges, 2002; Ulbrich et al., 2009; Wernli & Schwierz, 2006).

3.2 Sampling and Compositing Approach

We conduct cyclone-centered sampling of the MODIS and M2GMI fields at a resolution of 1^{o}. For M2GMI, we first regrid the fields from the native 0.5^{o} × 0.625^{o} grid to the 1^{o} × 1^{o} MODIS grid. For each cyclone we use bilinear interpolation to translate and regrid the daily fields onto a 4,000 km × 4,000 km region centered over the cyclone (Field & Wood, 2007). The cyclone-centered grid has 100 km horizontal grid spacing. We then average together the cyclones to generate annual and seasonal composites. For comparison to MODIS, the 2pm local time M2GMI AOD fields are sampled when there are valid 1^{o} × 1^{o} MODIS retrievals and MODIS CF <50%. The same compositing is applied to 24-hour daily mean M2GMI meteorological and aerosol fields without any filtering for clouds.

To examine how each midlatitude cyclone perturbs the distribution of aerosols relative to background conditions we generate a separate cyclone-centered grid at the same date and location of the original cyclone but instead using a 60-day running mean of each field smoothed with a 6^{o} wide boxcar average. Anomalies (e.g., ΔAOD) are given as the difference between the cyclone and its background ($\Delta AOD = AOD_{cyclone} - AOD_{background}$) or as the percent enhancement relative to background ($\Delta AOD = 100 \times (AOD_{cyclone} - AOD_{background}) / AOD_{background}$).

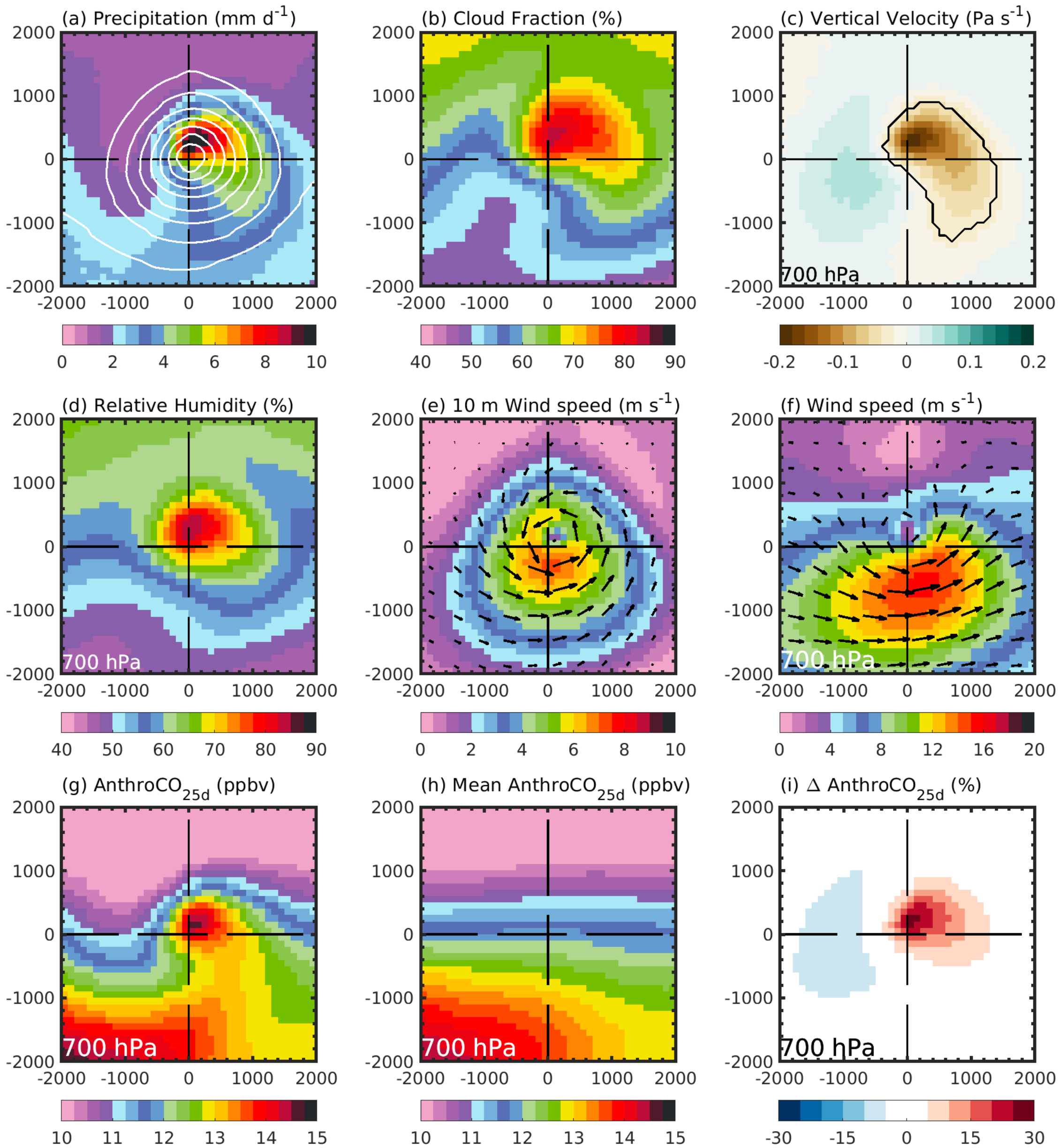

Figure 1. Annual mean composites of 27,707 midlatitude cyclones from M2GMI (2005-2018). (a) precipitation (mm d^{-1}), with sea-level pressure contours in white; (b) total cloud fraction (CF, %); (c) 700 hPa vertical velocity (ω, Pa s^{-1}); the black contour corresponds to the mean position of the WCB airstream; (d) 700 hPa relative humidity (%); (e) 10 m wind speed (u_{10m}, m s^{-1}), with vector winds represented by arrows; (f) 700 hPa wind speed (m s^{-1}), with vector winds represented by arrows; (g) 700 hPa AnthroCO$_{25d}$ (ppb); (h) Background 700 hPa AnthroCO$_{25d}$ (ppb); (i) 700 hPa AnthroCO$_{25d}$ anomaly. For each panel, the *x* and *y* axes labels represent the distance from the cyclone center (*x* = 0 and *y* = 0) in kilometers, with *x* increasing in the eastward direction and *y* increasing in the poleward direction.

Figure 1 shows the annual mean 2005-2018 NH midlatitude cyclone composites of M2GMI precipitation, CF, vertical velocity (ω) at 700 hPa, relative humidity (RH) at 700 hPa, 10 m wind speed (u_{10m}), and wind speed at 700 hPa. Maximum precipitation (>8 mm d^{-1}) occurs near the center of the cyclone and curves to the southwest to create the characteristic comma shape (e.g., Field & Wood, 2007; Naud et al., 2017; Figure 1a). Strongest ascent (minimum ω) associated with the WCB also occurs near the center of the cyclone co-located with the region of precipitation. In this region of the composite, ω values of -0.2 Pa s^{-1} represent about 175 hPa of overall ascent extrapolated to a 24-hour period (Figure 1c). The most extensive CF (>75%) in the composite occurs where the WCB turns cyclonically and creates the "cloud head" as viewed in satellite imagery (Catto et al., 2010; Figure 1b). The air at 700 hPa has high RH (>80%) near the center of the composite (Figure 1d). The flow near the surface is cyclonic, with u_{10m} >6 m s^{-1} just to the south of the cyclone center (Figure 1e). At 700 hPa wind speeds reach as high as 18 m s^{-1} south of the cyclone center (Figure 1f).

Figures 1g-i show the composites of 700 hPa AnthroCO$_{25d}$ from M2GMI. Both the cyclone and background composites display the largest concentrations of AnthroCO$_{25d}$ in the southwest of the domain, reflecting outflow from the polluted continental boundary layer. The cyclone composite also shows that as the WCB ascends and wraps into the cyclone center, it carries elevated AnthroCO$_{25d}$ (13-15 ppbv) offshore and into the free troposphere (Figure 1g). The ΔAnthroCO$_{25d}$ composite highlights that cyclone WCBs enhance mean AnthroCO$_{25d}$ in the lower free troposphere by 15-30% compared to background conditions (Figure 1i). The composites also display a 5-10 % reduction in AnthroCO$_{25d}$ behind the cyclone as cleaner air is transported equatorward both from higher altitudes and latitudes in the DI.

4 Aerosol Optical Depth Composites

4.1 Annual Mean and Seasonal AOD Composites

Composites of MODIS Aqua AOD exhibit a pattern of elevated AOD to the east of the cyclone center in the WCB, with values of 0.13-0.16 (Figure 2a). Relative to background conditions, MODIS AOD is enhanced by 20-45% in the WCB, coinciding with the regions of enhanced vertical ascent, precipitation, and clouds (Figure 1). M2GMI predicts slightly higher AOD values (0.14-0.18) but captures the cyclone-wide features observed by MODIS quite well ($r = 0.88$; Figure 2a-d), with enhancements of 30-50% above background. MODIS and M2GMI show similar decrease in AOD (ΔAOD = -25%) to the west of the cyclone center in the DI (Figure 2a-d). These composites are based only on cloud-free grid cells within each cyclone, thus limiting the number of MODIS points available for the composites (Figure S2). Despite this, enough points remain to obtain coherent patterns of AOD.

MODIS fAOD reaches values of 0.07-0.09 to the east and northeast of the cyclone center (Figure 3e). In this region M2GMI captures similar values of fAOD (0.07-0.1) but across a larger area that is spread out to the east (Figure 3g). For both MODIS and M2GMI, the fine mode fraction (FMF = fAOD / AOD) has values of 0.5-0.6 in the WCB. This is consistent with Naud et al. (2016) who found the breakdown of MODIS fine and coarse AOD to be about equal in the warm sector. Both MODIS and M2GMI show fAOD enhancements of 20-40% relative to background fAOD (Figures 3f,h). In addition, cAOD is maximum (>0.08) near the center of the composite, where it is enhanced by more than a factor of two relative to background cAOD (Figures 3i-l). We have applied this same procedure to the AOD from MODIS on the Terra satellite, finding similar results (Figure S3), with MODIS Terra AOD values being slightly larger than Aqua (e.g., Wei et al., 2019b).

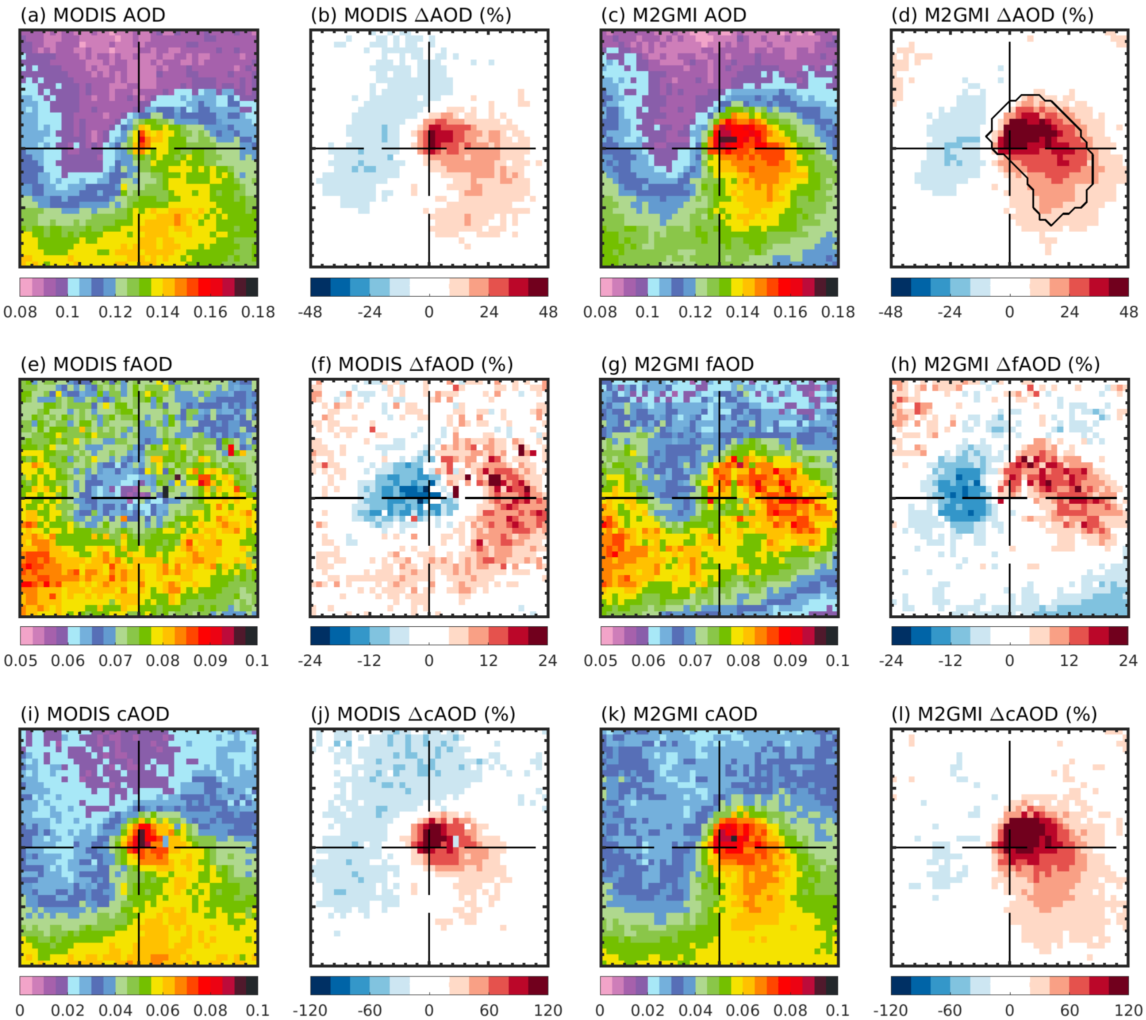

Figure 2. Midlatitude cyclone composites of AOD, fine AOD (fAOD), coarse AOD (cAOD), and their enhancements for MODIS Aqua (a, b, e, f, i, and j) and M2GMI (c, d, g, h, k, and l). Enhancements are expressed as a percent relative to the respective backgrounds. The M2GMI AOD is sampled at the Aqua overpass time only when there are valid MODIS AOD observations (section 3.2). The black contour in Figure 3d corresponds to the WCB region as defined in section 4.1. The composites shown represent the same cyclones shown in Figure S1 and Figure 1.

For each cyclone, we identify the WCB as the outermost closed 700 hPa ω contour enclosing an ω minimum (ascent maximum) within 1,000 km of the cyclone center. The black contour in Figure 2d shows the area of the WCB when the identification procedure is carried out on the ω composite from Figure 1c. We calculate the mean AOD in the WCB region of each cyclone and the resulting seasonal cycle in MODIS and M2GMI AOD is shown in Figure 3. The WCB AOD observed by MODIS reaches its maximum in April and May, with a secondary maximum in July. M2GMI reproduces the observed MODIS AOD well (r = 0.97; NMB = 6%). When expressed as a percent enhancement relative to background (Figure 3c) we find that MODIS AOD is enhanced by 65% on average, with the highest enhancements occurring in July (90%) when background AOD is at a minimum. Note that extracting AOD values within individual WCBs yields values larger than seen in the Figure 2 composites as application of the identification criteria to each cyclone individually allows the location of the WCB to vary. We find that fAOD accounts for 68% of the WCB ΔAOD annually and has the same seasonal cycle as ΔAOD, maximizing in spring-summer (Figure 3). During December and January, when cAOD reaches its maximum value, it accounts for half of AOD. We find similar results for MODIS Terra (Figure S4). The M2GMI simulation captures the observed seasonality in WCB AOD, the contributions from coarse and fine AOD, and their respective enhancements relative to background (Figures 3 and S4).

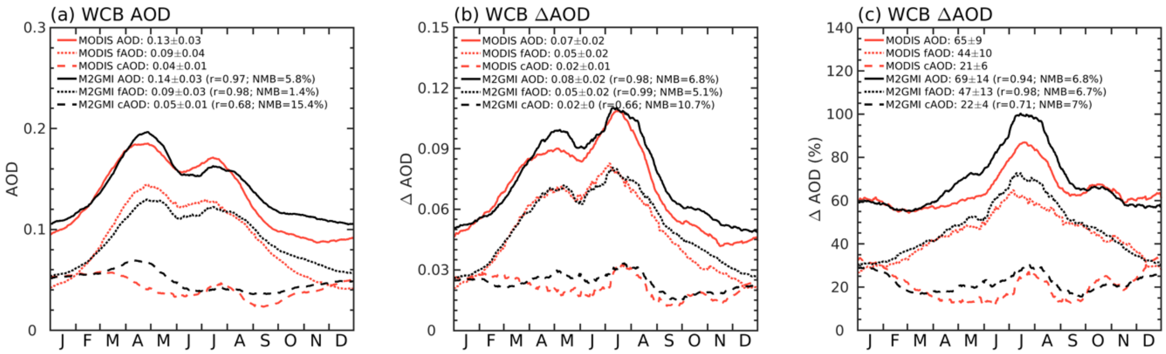

Figure 3. (a) Composite seasonal cycle for AOD, fAOD, and cAOD in the warm conveyor belt of individual cyclones (section 4.1). (b) Composite seasonal cycle for AOD, fAOD, and cAOD anomalies. (c) Same as (b) but expressed a percent relative to the total AOD background. Values are shown for MODIS Aqua (orange lines) and M2GMI (black lines). A 40-day boxcar smoothing has been applied to each time series. Annual mean values for each timeseries are also given in the legend.

4.2 Contributions of Aerosol Species to AOD Composites

We now examine composites of the M2GMI simulation to understand the relative contribution of individual aerosol species to the midlatitude cyclone AOD composites (Figure 4). Here, we use daily mean M2GMI values instead of the 2pm Aqua overpass time. Furthermore, we do not apply any sampling relative to MODIS data availability or CF such that the composites include both cloudy and cloud-free regions of the midlatitude cyclones. Figure 4a shows that the WCB stands out as a region of large AOD (>0.2) to the east of the cyclone center, with values that are 25-30% larger than those in Figure 2c due the inclusion of cloudy regions.

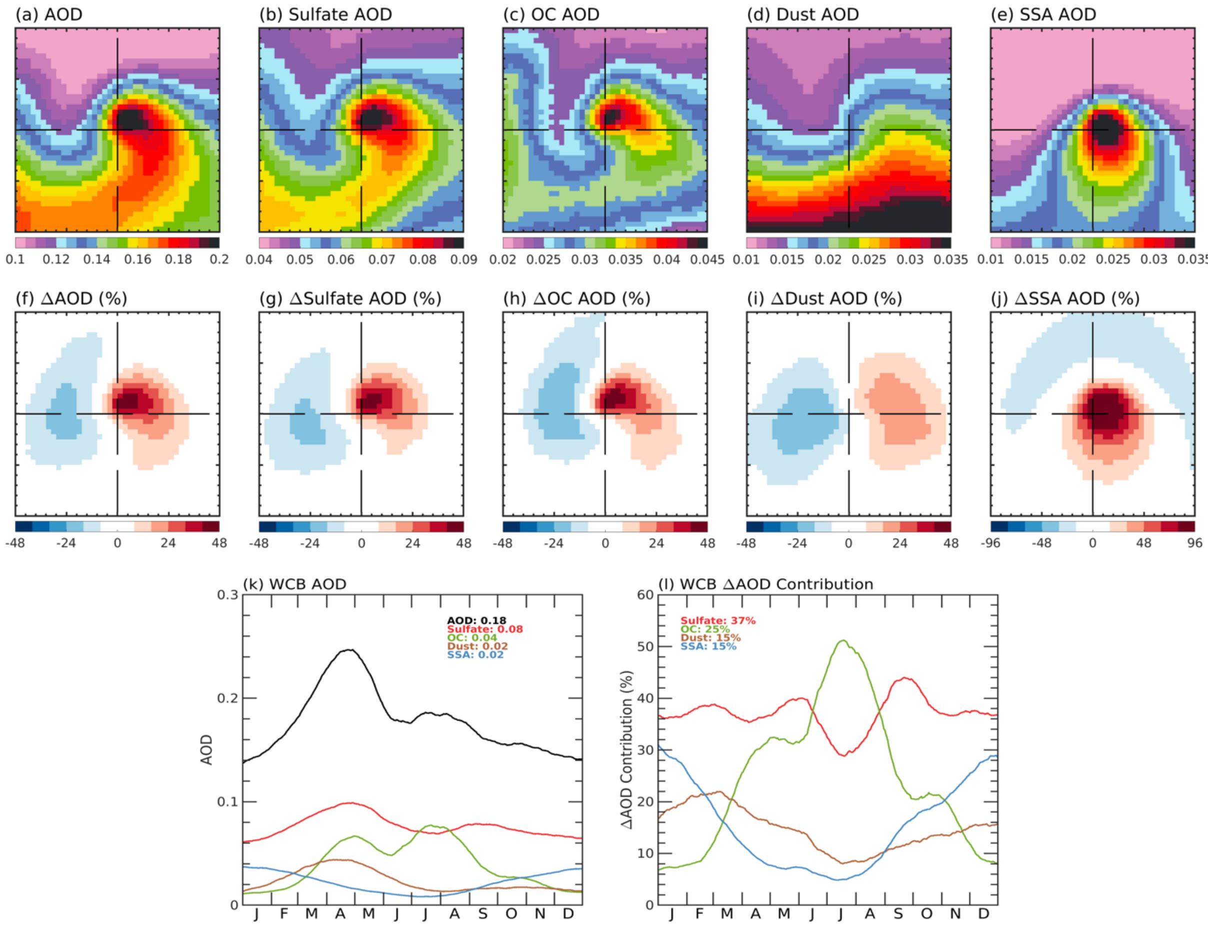

Figure 4. Top row: midlatitude cyclone composites of M2GMI AOD for (a) total, (b) sulfate, (c) organic carbon, (d) dust, (e) SSA. Middle row: Same as top row but expressed as anomalies relative to background values. For individual aerosol species, the background is defined relative to that species (i.e., $\Delta\ AOD_{dust} = 100 \times (AOD_{dust} - AOD_{dust,\ background}) / AOD_{dust,\ background}$). Bottom row: seasonal cycle of WCB M2GMI AOD (k) and contributions of individual aerosol species to ΔAOD (l). The timeseries have been smoothed with a 40-day boxcar average and annual mean values for each species are given in the legend. Black carbon and nitrate aerosol (not shown) together contribute less than 10% of the ΔAOD.

The cyclone composites of sulfate and OC display similar shapes (Figures 4b,g and 4c,h), reflecting vertical transport of these aerosols and/or their precursors in the WCB. Dust enhancements maximize at 30% in a region extending to the east of the cyclone center (Figure 4d,i), while SSA is strongly enhanced near the cyclone center (Figure 4e,j). Figure 4l shows sulfate accounts for 37% of the ΔAOD, followed by OC (25%), dust (15%), and SSA (15%).

Figure 4k helps interpret the seasonality of WCB AOD observed by MODIS: the spring maximum is driven by sulfate, with smaller contributions from OC and dust, while the summer secondary maximum follows the seasonality of OC, with smaller contributions from sulfate. In M2GMI the summer maximum in OC is due to a combination of high emissions of OC from fires and of biogenic volatile organic compounds. SSA AOD maximizes in winter and reaches its lowest values in summer, following the seasonality of u_{10m} in midlatitude cyclones (Field & Wood, 2007).

4.3 Variability of AOD Enhancements in Cyclone WCBs

We now examine variability in total AOD by storm track region, analyzing 11,140 midlatitude cyclones with centers in the N. Pacific (30-80º N, 110ºE – 120ºW) and 8,724 cyclones in the N. Atlantic (30-80ºN, -90ºE – 20ºE). We find that N. Pacific midlatitude cyclones have AODs that are 60% larger compared to N. Atlantic cyclones (Figure 5), consistent with larger emissions of pollution from Asia relative to North America. This inter-basin difference is seen in both the MODIS and M2GMI composites with M2GMI overestimating AOD in N. Pacific cyclones by 11%. M2GMI underestimates AOD in N. Atlantic cyclones by 8%.

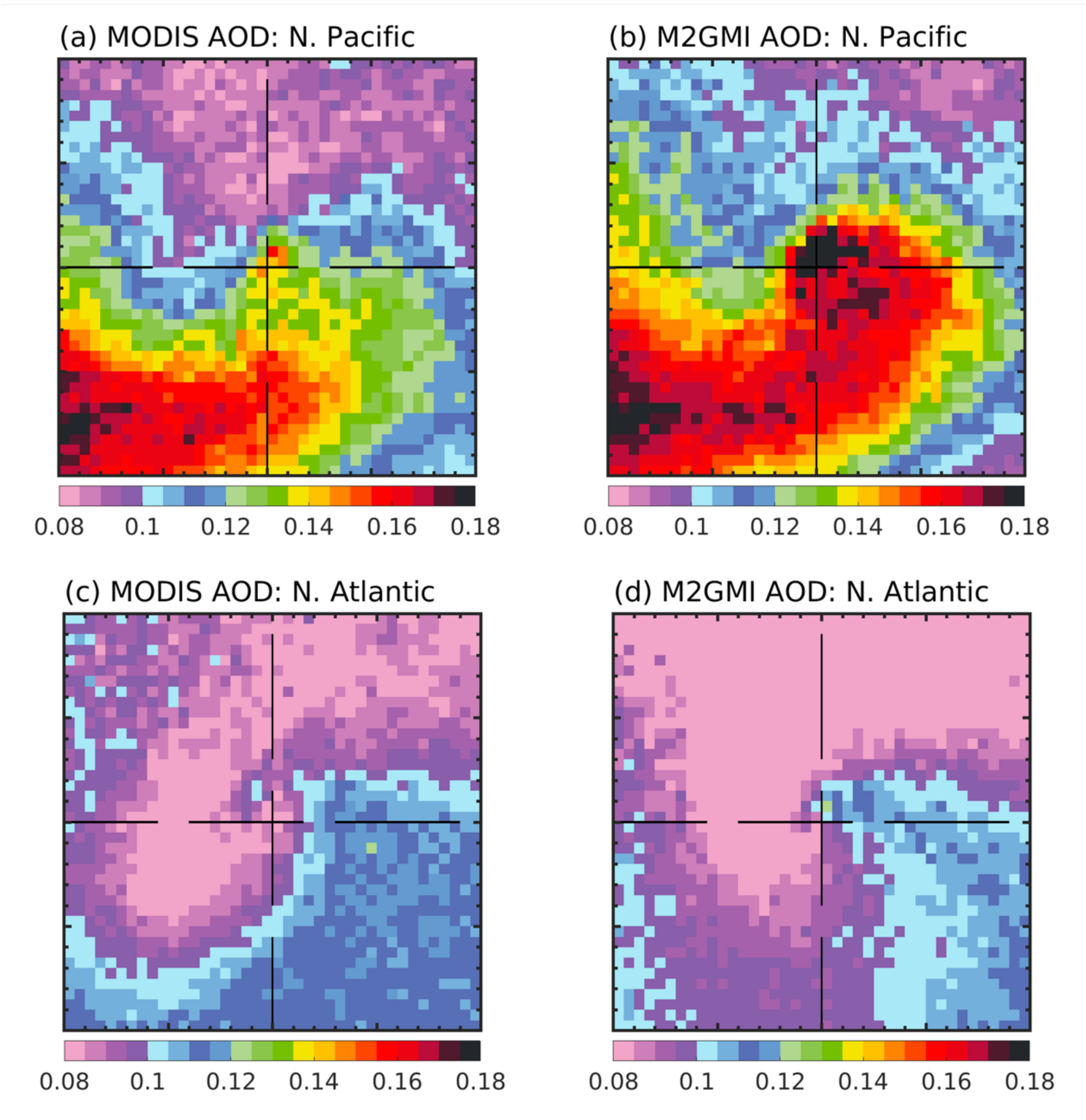

Figure 5. Midlatitude cyclone AOD ΔAOD in the (a,b) N. Pacific (11,140 cyclones) and (c,d) N. Atlantic (8,724 cyclones) for MODIS (left) and M2GMI (right). M2GMI AOD is sampled at the Aqua overpass time only when there are valid MODIS AOD observations and CF <50% (section 3.2).

To further characterize storm track variability in the WCB of midlatitude cyclones, we examine how AOD varies with 700 hPa $\Delta AnthroCO_{25d}$, which we use as a proxy for pollution. We grouped cyclone WCBs in 5% $\Delta AnthroCO_{25d}$ bins. In the N. Pacific storm track MODIS AOD increases with increasing WCB pollution levels, nearly doubling from 0.11 to 0.19 (Figure 6a). This relationship is much weaker for N. Atlantic WCBs, with AOD increasing from 0.09 to 0.11. Most of the increase in AOD with increasing pollution is due to increases in fAOD (Figure 6b), while cAOD remains nearly invariant (Figure 6c). In WCBs with negative $\Delta AnthroCO_{25d}$, which correspond to midlatitude cyclones drawing air from the clean marine boundary layer, fAOD constitutes just over half of the AOD whereas for cyclones with large $\Delta AnthroCO_{25d}$ it constitutes nearly 80%. M2GMI captures the observed relationships reasonably well, but overestimates N. Pacific AOD and fAOD by 6-20% (Figure 6).

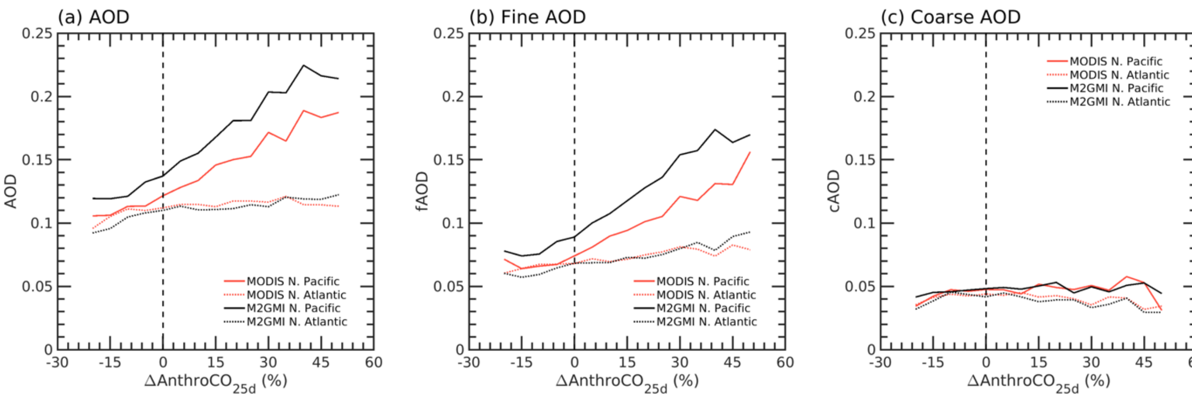

Figure 6. Relationship between AOD and anthropogenic pollution ($\Delta AnthroCO_{25d}$) in the WCB of individual cyclones: (a) total AOD, (b) fAOD, and (c) cAOD. Cyclones have been grouped in 5% bins based on M2GMI $\Delta AnthroCO_{25d}$. Values for MODIS (orange lines) and M2GMI (black lines) are separated between the N. Pacific (solid lines) and N. Atlantic (dashed lines) basins.

The dependence of individual aerosol species in M2GMI with $\Delta AnthroCO_{25d}$ (Figure S5) shows that sulfate explains most of the AOD and fAOD differences between the N. Pacific and N. Atlantic storm tracks. In N. Pacific midlatitude cyclones, M2GMI shows that sulfate, OC, and dust all increase with $\Delta AnthroCO_{25d}$ – reflecting their continental origin. Sulfate accounts for 65% of the strong increase in AOD with increasing pollution in the N. Pacific with OC and dust accounting for 14% and 7%, respectively. SSA displays behavior opposite to that of the continental aerosols, with a small decrease in AOD as $\Delta AnthroCO_{25d}$ increases. Together, the opposite behavior of dust and SSA with pollution help explain the near invariance of cAOD with increasing $\Delta AnthroCO_{25d}$ (Figure 6c).

5 Vertical Distribution of Aerosol Extinction and Mass

Figure 7 shows composites of M2GMI total aerosol extinction, aerosol extinction enhancement, aerosol dry mass enhancement (ΔM_d), ω, and RH between the surface and 8 km altitude. To calculate the overall ΔM_d, the individual component dry mass enhancements have been weighted by their contribution to the background AOD in M2GMI. Aerosol extinction is enhanced by more than 20-40% through a deep layer extending from the surface to 8 km in the WCB (Figure 7). This enhancement in extinction coincides with strong upward motion and high RH at all levels. As the WCB ascends above 1-2 km, it begins to spread out to the east and northeast, wrapping cyclonically with the DI, which transports cleaner air (Figure 7). This is indicative of our selection of midlatitude cyclones being dominated by stronger, cut-off cyclones (Whitaker et al., 1988).

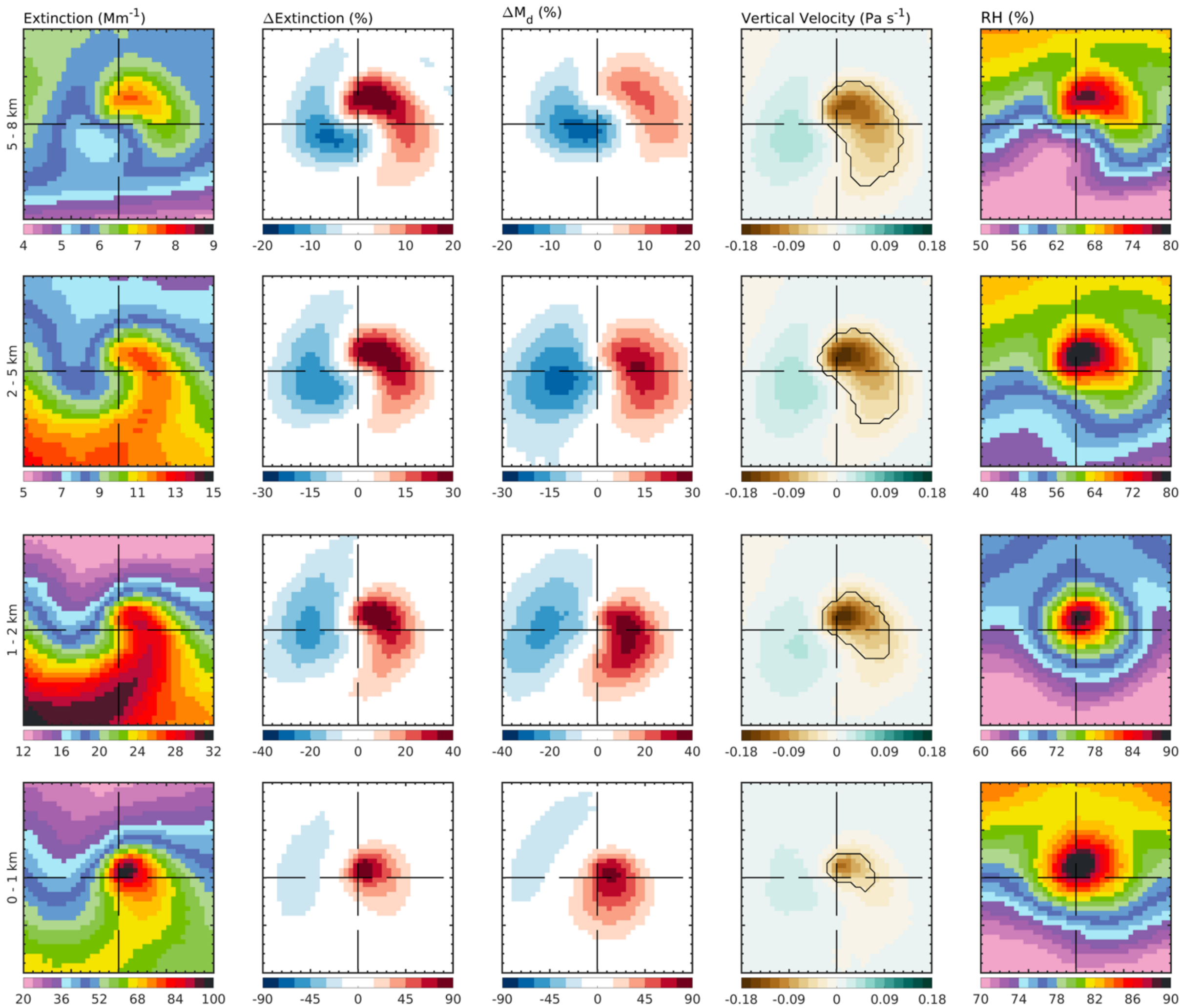

Figure 7. Composites of M2GMI layer mean total aerosol extinction (first column; Mm^{-1}), Δ extinction (second column; %), aerosol dry mass enhancement (ΔM$_d$, third column; %), vertical velocity (ω, fourth column; Pa s^{-1}), and RH (fifth column, %) for 2005-2018 NH midlatitude cyclones. The ΔM$_d$ has been weighted according to each aerosol component's contribution to the background extinction (section 5). The altitude layers correspond to 5-8 km (top row), 2-5 km (second row), 1-2 km (third row), and 0-1 km (bottom row). The black contours in the third column represent the average extent of the warm conveyor belt airstream (as defined in section 4.1 of the text).

Vertical profiles of M2GMI extinction in the WCB show that below 1km in altitude, the extinction is dominated by sulfate and SSA, which together account for ~75% of the enhancement in total extinction (Figure S6). SSA extinction rapidly declines away from the surface, but sulfate is the largest contributor to extinction throughout much of the profile, followed by OC and dust. The contribution of dust to the total extinction enhancement reaches 20% between 2.5-5.5 km. These results are consistent with Luan & Jaeglé (2013), who found sulfate export to occur at altitudes between 1-3 km and 2-6 km off North America and Asia, respectively. They are also consistent with He et al. (2012) who noted elevated concentrations of sulfate precursors in the free troposphere between 2-4 km over China in spring. While dust aerosols may be lifted in the WCB, much of the signature in the profiles likely comes from horizontal export of dust from high altitude desert regions in Asia (e.g., Eguchi et al., 2009; Huang et al., 2008).

How much of the enhanced AOD in the WCB is due to humidification as opposed to increased aerosol mass? To first order, ΔExtinction is equal to the sum of ΔM_d and the enhancement in aerosol mass extinction efficiency ($\Delta\beta$), which includes humidification effects (SI Text 1). Near the surface, ΔExtinction and ΔM_d display similar values, reaching 90% (Figure 7), which implies only a small contribution of humidification effects in the already very humid boundary layer. As the WCB ascends, the two enhancements begin to diverge, with ΔM_d decreasing more rapidly than ΔExtinction, indicative of an increasing contribution of humidification effects on extinction. For example, in the 5-8km layer ΔExtinction maximizes at 20% while ΔM_d reaches only 10-12% (Figure 7). Overall, we find that aerosol growth by humidification accounts for ~40% of the ΔAOD in cyclone WCBs (Figure S7).

6 Midlatitude Cyclone Sea Salt Aerosol Emissions and Net Effect on NH Aerosols

6.1 Midlatitude Cyclones as a Source of SSA

We now quantify the contribution of midlatitude cyclones as a source of SSA. Figure 8a shows the M2GMI mean composite of SSA emissions for all NH midlatitude cyclones in 2005-2018. A core of large emissions (>40 kg km^{-2} d^{-1}) occurs 100-500 km south of the cyclone center. We calculate total SSA emissions in the high wind speed region (u_{10m} >5 m s^{-1}) within 2,000 km of the cyclone center for the composite and find that, on average, a NH midlatitude cyclone leads to SSA emissions of 0.179 Tg d^{-1}. We apply the same approach to calculate SSA emissions for each individual midlatitude cyclone and show the resulting seasonal cycle in Figure 8b. Annually, high winds associated with midlatitude cyclones emit 355 Tg yr^{-1}, compared to the total SSA emissions of 594 Tg yr^{-1} in the 30-80°N region. Thus, midlatitude cyclones account for 60% of the total SSA emissions. The region of high cyclone winds over which we integrate SSA emissions covers 40% of the NH ocean area annually (Figure S8). Therefore, midlatitude cyclones account for more than twice as much SSA emissions per surface area as the rest of the NH oceans. SSA emissions from midlatitude cyclones maximize in winter (1.5-1.8 Tg d^{-1}) and decrease to a summer minimum of 0.3-0.5 Tg d^{-1}. This seasonal variability follows from the seasonal variability in u_{10m} (Figure S8).

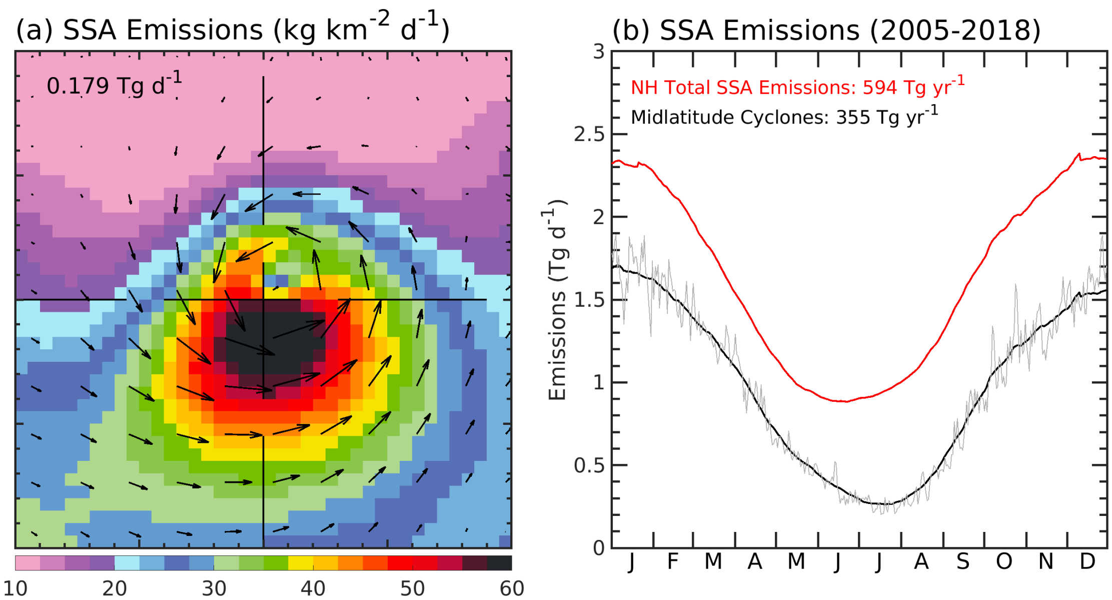

Figure 8. (a) Cyclone composite of SSA emissions (kg km^{-2} d^{-1}). The mean daily composite SSA emissions calculated as in section 6.1 is given in the top left of the panel. Composite u_{10m} vector winds are represented by arrows. (b) Annual cycle of NH midlatitude cyclone SSA emissions calculated over the high wind-speed region for each cyclone (u_{10m} >5 m s^{-1}, 30-80°N). Daily emissions are in gray while the black line shows emissions smoothed with a 40-day boxcar average). The multiyear mean SSA emissions for 30-80 ° N emissions is shown in red.

6.2 Net effect of Midlatitude Cyclones on NH Aerosol Budgets

We use the M2GMI simulation to isolate the contribution of midlatitude cyclone WCBs to the budgets of sulfate, OC, and dust over the NH midlatitude oceans, separating the N. Pacific (30 – 70°N, 140°E – 120°W) and N. Atlantic (30 – 70°N, 80°W – 15°W) basins. For each day and basin, we extract the basin-wide burden, chemical production (for sulfate), dry+wet deposition, emission, and horizontal fluxes. We do the same for individual midlatitude cyclones, using WCBs defined by 700 hPa ω (section 4.1). We also average over the 2005-2018 period to construct a mean annual cycle for both the entire basin and cyclones.

Figure 9 summarizes the 2005-2018 annual mean budgets for sulfate, OC, and dust. Basin-wide fluxes are represented by solid arrows while midlatitude cyclone WCBs are denoted by dashed arrows. Comparing the basin-wide and cyclone values in the N. Pacific, we find that midlatitude cyclone WCBs contribute 16-20% of the sulfate, OC, and dust horizontal fluxes along 140°E. The contribution of WCB to fluxes into the N. Pacific maximize in spring at 30%. The seasonality and contribution of WCBs to fluxes along 80°W in the N. Atlantic is similar (18-22%). On the eastern edge of the basins, cyclone WCBs contribute 14-23% of fluxes out of the NH basins (maximizing at 20-30% in spring). In addition, midlatitude cyclones account for a significant fraction of the aerosol flux to polar regions, with contributions ranging from 18-24% for sulfate, 19-31% for OC, and 26-27% for dust.

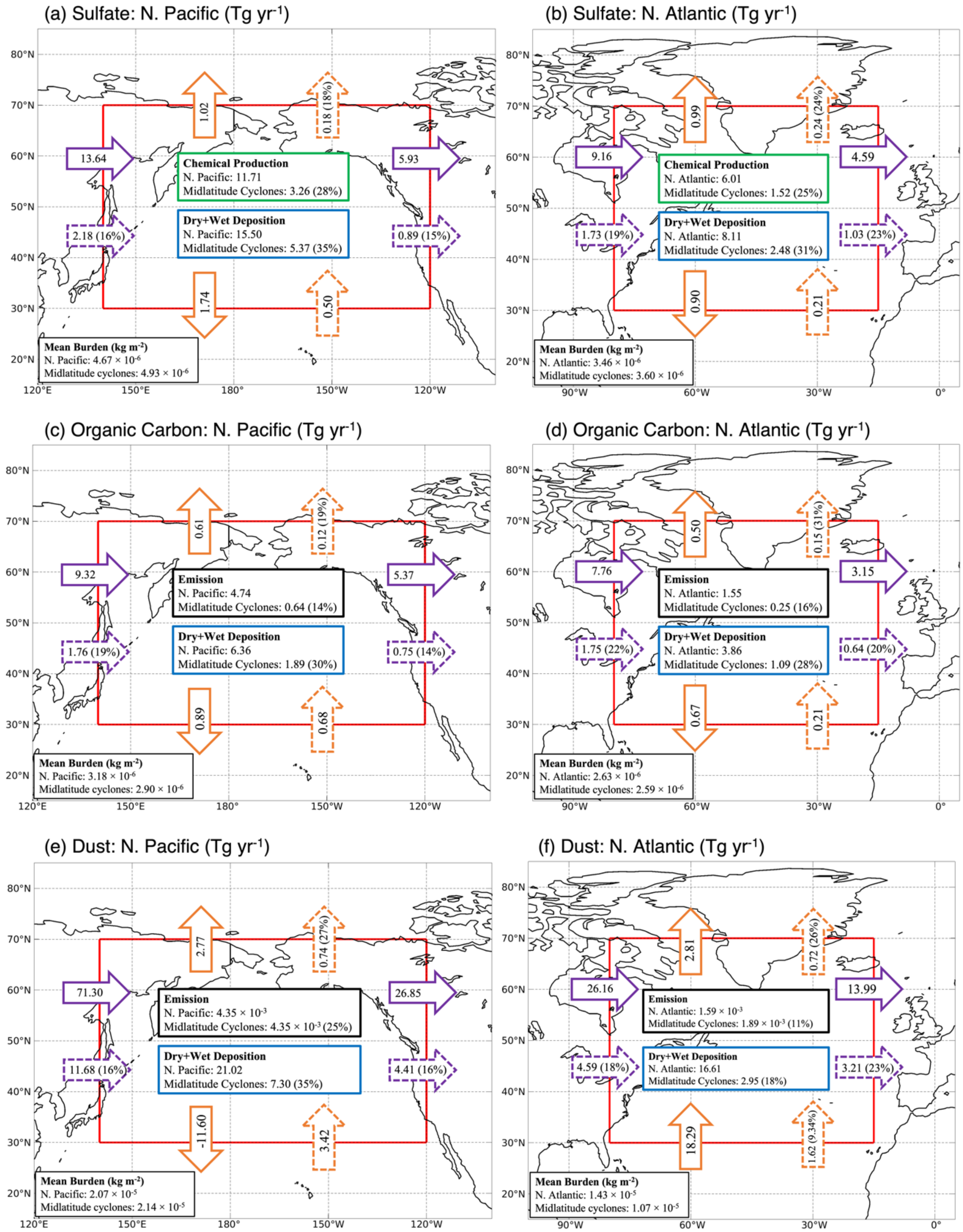

Figure 9. Annual mean 2005-2018 aerosol budgets within northern hemisphere ocean basins (units Tg yr^{-1}). (a,c,e) N. Pacific basin (30 – 70°N, 140°E – 120°W, red outline). (b,d,f) N. Atlantic basin (30 – 70°N, 80°W – 15°W, red outline). In each panel solid arrows represent horizontal advective fluxes through the boundaries, while dashed arrows represent fluxes associated with midlatitude cyclone WCBs. The annual mean basin-wide and midlatitude cyclone burden (units kg m^{-2}) are given in the bottom left of each panel.

Large-scale precipitation associated with WCBs results in efficient dry+wet deposition of aerosols, accounting for ~30% of the sulfate, OC, and dust deposition over the N. Pacific and N. Atlantic basins. This contribution varies seasonally, ranging from 50% in spring to 20% in summer. In the N. Pacific, WCBs cover 18% of the area annually while in the N. Atlantic they cover 15% of the area annually. Therefore, midlatitude cyclone WCBs are about twice as efficient at scavenging aerosols as the broader NH basins.

Annually in the N. Pacific, we find WCBs lead to 3.26 Tg yr^{-1} of sulfate production, 80% of which occurs through aqueous SO_2 oxidation in the extensive cyclone cloud cover. Basin-wide production of sulfate aerosol is 11.71 Tg yr^{-1} in the N. Pacific, meaning WCBs contribute 28% to the total. WCB contributions range from 10% (summer) to 40% (spring). Comparing these values to the deposition and fluxes of sulfate is consistent with its evolution following the conceptual models put forth in Brock et al. (2004) and Dunlea et al. (2009). Cyclone WCBs efficiently scavenge sulfate aerosol such that the increases in WCB sulfate mass relative to the basin-wide average are due to export of SO_2 followed by its oxidation in midlatitude cyclones. WCBs contribute similarly to sulfate production in the N. Atlantic (1.52 Tg yr^{-1} resulting in a 25% contribution).

7 Conclusions

Our analysis systematically examined AOD and aerosol distributions in midlatitude cyclones and linked processes in the WCB and broader cyclone environment to aerosol emissions and export to the global atmosphere. The composites of 27,707 NH midlatitude cyclones over a 14-year period show a 25-45% increase in AOD observed by MODIS to the east of the cyclone center. These enhancements are co-located with heavy precipitation, extensive cloud cover, vertical motions, and high RH in the cyclone WCB. The M2GMI simulation shows a 30-50% increase in AOD in the same region. AOD and ΔAOD in cyclone WCBs maximize in spring due to a large contribution (>70% of the total) from fine mode aerosols. Annually, fine aerosols accounts for 70% of the ΔAOD in MODIS and 63% in M2GMI. Overall, we find the M2GMI simulation captures the magnitude and seasonality of the MODIS observations.

M2GMI composites of individual aerosol species AOD show that cyclones enhance AOD by up to 40% for sulfate, 50% for OC, 25% for dust, and 130% for SSA. The contribution of sulfate to the total ΔAOD is consistent throughout the year at 30-40%. The contribution of the other components shows large variability. The contribution of SSA ranges from 30% in fall-winter to <10% in summer while the contribution of OC ranges from <10% in winter to >50% in July and August. The contribution of dust maximizes at 20% in spring. Larger pollutant emissions in Asia lead to 60% larger AODs in N. Pacific WCBs than those in the N. Atlantic. This also leads to a stronger relationship between WCB pollution and sulfate and OC AODs in N. Pacific WCBs.

We find that the high surface winds associated with midlatitude cyclones account for 355 Tg yr^{-1} of SSA emissions annually, which constitutes 60% of the 30–80° N SSA emissions. Our compositing approach also highlights the net effect of midlatitude cyclones on aerosol budgets over the NH oceans. WCBs facilitate export of aerosols to and from the N. Pacific and N. Atlantic basins, accounting for ~16-22% of the horizontal advective fluxes on the western and eastern boundaries, and ~18-31% of transport to polar regions. We find that largescale precipitation in cyclone WCBs efficiently removes aerosols such that they contribute 27-33% to deposition over the N. Pacific and N. Atlantic basins while only covering 15-18% of the area. In addition, WCB export of SO_2 followed by its in-cloud oxidation accounts for 25-28% of the total chemical production of sulfate in the N. Pacific and N. Atlantic basins.

Aerosols remain a highly uncertain part of the climate future (Szopa et al., 2021) particularly due to changing anthropogenic emissions. As societies transition away from energy sources that emit greenhouse gases, it is likely that anthropogenic aerosol emissions will also decrease (Larson & Portmann, 2019). Nevertheless, results from the Coupled Model Intercomparison Project Phase 6 suggest increases in urban particulate matter even in scenarios with some climate mitigation actions (Turnock et al., 2020). In addition, transport pathways may change in the future as the spatiotemporal variability of midlatitude cyclones changes. While disagreement exists in projections of the NH storm tracks, one consistent projection is a seasonally non-uniform poleward shift (Simpson et al., 2014) coupled with an overall reduction in frequency (Chang et al., 2012). Recent projections also suggest an increase in midlatitude cyclone precipitation under future climate scenarios (Catto et al., 2019) that could act to increase aerosol removal during transport. Taken together, these projections may suggest an overall reduction in aerosol export to the global atmosphere by cyclone WCBs with a simultaneous increase in aerosol abundances for the most polluted cyclones.

Acknowledgements

This work was supported under NSF award number 1901786. MERRA-2 GMI is supported by the NASA Modeling, Analysis, and Prediction (MAP) program and the high-performance computing resources were provided by the NASA Center for Climate Simulation (NCCS).

Open Research

MODIS collection 6.1 observations used in this study are available for download at the following: https://ladsweb.modaps.eosdis.nasa.gov/archive/allData/61/. The MERRA-2 GMI data used in this study are a product of the NASA GMAO and are available at the following: https://portal.nccs.nasa.gov/datashare/merra2_gmi/. The cyclone-centered grids used in the compositing are available in netCDF format upon request.

8 References

Alfaro, C., & Gomes, L. (2001). Modeling mineral aerosol production by wind erosion : Emission Particles enough. *Geophysical Research*, *106*(D16), 75–84.

Andreae, M. O., & Crutzen, P. J. (1997). Atmospheric aerosols: Biogeochemical sources and role in atmospheric chemistry. *Science*, *276*(5315), 1052–1058. https://doi.org/10.1126/science.276.5315.1052

Baker, A. R., Kelly, S. D., Biswas, K. F., Witt, M., & Jickells, T. D. (2003). Atmospheric deposition of nutrients to the Atlantic Ocean. *Geophysical Research Letters*, *30*(24), 2–5. https://doi.org/10.1029/2003GL018518

Bian, H., Chin, M., Hauglustaine, D. A., Schulz, M., Myhre, G., Bauer, S. E., … Tsyro, S. G. (2017). Investigation of global particulate nitrate from the AeroCom phase III experiment. *Atmospheric Chemistry and Physics*, *17*(21), 12911–12940. https://doi.org/10.5194/acp-17-12911-2017

Bian, H., Froyd, K., Murphy, D. M., Dibb, J., Darmenov, A., Chin, M., … Smirnov, A. (2019). Observationally constrained analysis of sea salt aerosol in the marine atmosphere. *Atmospheric Chemistry and Physics*, *19*(16), 10773–10785. https://doi.org/10.5194/acp-19-10773-2019

Booth, J. F., Naud, C. M., & Jeyaratnam, J. (2018). Extratropical Cyclone Precipitation Life Cycles: A Satellite-Based Analysis. *Geophysical Research Letters*, *45*(16), 8647–8654. https://doi.org/10.1029/2018GL078977

Brock, C. A., Hudson, P. K., Lovejoy, E. R., Sullivan, A., Nowak, J. B., Huey, L. G., … Wilson, J. C. (2004). Particle characterictics following cloud-modified transport from Asia to North America. *Journal of Geophysical Research D: Atmospheres*, *109*(23), 1–17. https://doi.org/10.1029/2003JD004198

Browning, K. A. (1997). The dry intrusion perspective of extra-tropical cyclone development. *Meteorological Applications*, *4*(4), S1350482797000613. https://doi.org/10.1017/S1350482797000613

Browning, K. A., & Roberts, N. M. (1994). Structure of a frontal cyclone. *Quarterly Journal of the Royal Meteorological Society*, *120*(520), 1535–1557. https://doi.org/10.1002/qj.49712052006

Catto, J. L., Ackerley, D., Booth, J. F., Champion, A. J., Colle, B. A., Pfahl, S., … Seiler, C. (2019). The Future of Midlatitude Cyclones. *Current Climate Change Reports*, *5*(4), 407–420. https://doi.org/10.1007/s40641-019-00149-4

Catto, J. L., Shaffrey, L. C., & Hodges, K. I. (2010). Can climate models capture the structure of extratropical cyclones? *Journal of Climate*, *23*(7), 1621–1635. https://doi.org/10.1175/2009JCLI3318.1

Chang, E. K. M., Guo, Y., & Xia, X. (2012). CMIP5 multimodel ensemble projection of storm track change under global warming. *Journal of Geophysical Research Atmospheres*, *117*(23), 1–19. https://doi.org/10.1029/2012JD018578

Chin, M., Diehl, T., Tan, Q., Prospero, J. M., Kahn, R. A., Remer, L. A., … Torres, O. (2014). Multi-decadal aerosol variations from 1980 to 2009: A perspective from observations and a global model. *Atmospheric Chemistry and Physics*, *14*(7), 3657–3690. https://doi.org/10.5194/acp-14-3657-2014

Chin, Mian, Diehl, T., Dubovik, O., Eck, T. F., Holben, B. N., Sinyuk, A., & Streets, D. G. (2009). Light absorption by pollution, dust, and biomass burning aerosols: A global model study and evaluation with AERONET measurements. *Annales Geophysicae*, *27*(9), 3439–3464. https://doi.org/10.5194/angeo-27-3439-2009

Chin, Mian, Ginoux, P., Kinne, S., Torres, O., Holben, B. N., Duncan, B. N., … Nakajima, T. (2002). Tropospheric aerosol optical thickness from the GOCART model and comparisons with satellite and sun photometer measurements. *Journal of the Atmospheric Sciences*, *59*(3 PT 1), 461–483. https://doi.org/10.1175/1520-0469(2002)059<0461:taotft>2.0.co;2

Colarco, P., Da Silva, A., Chin, M., & Diehl, T. (2010). Online simulations of global aerosol distributions in the NASA GEOS-4 model and comparisons to satellite and ground-based aerosol optical depth. *Journal of Geophysical Research Atmospheres*, *115*(14). https://doi.org/10.1029/2009JD012820

Ding, A., Wang, T., Xue, L., Gao, J., Stohl, A., Lei, H., … Zhang, X. (2009). Transport of north China air pollution by midlatitude cyclones: Case study of aircraft measurements in summer 2007. *Journal of Geophysical Research Atmospheres*, *114*(8), 1–16. https://doi.org/10.1029/2008JD011023

Duncan, B. N., Strahan, S. E., Yoshida, Y., Steenrod, S. D., & Livesey, N. (2007). Model study of the cross-tropopause transport of biomass burning pollution. *Atmospheric Chemistry and Physics*, *7*(14), 3713–3736. https://doi.org/10.5194/acp-7-3713-2007

Dunlea, E. J., Decarlo, P. F., Aiken, A. C., Kimmel, J. R., Peltier, R. E., Weber, R. J., … Jimenez, J. L. (2009). Evolution of Asian aerosols during transpacific transport in INTEX-B. *Atmospheric Chemistry and Physics*, *9*(19), 7257–7287. https://doi.org/10.5194/acp-9-7257-2009

Eckhardt, S., Stohl, A., Wernli, H., James, P., Forster, C., & Spichtinger, N. (2004). A 15-year climatology of warm conveyor belts. *Journal of Climate*, *17*(1), 218–237. https://doi.org/10.1175/1520-0442(2004)017<0218:AYCOWC>2.0.CO;2

Eguchi, K., Uno, I., Yumimoto, K., Takemura, T., Shimizu, A., Sugimoto, N., & Liu, Z. (2009). Trans-pacific dust transport: Integrated analysis of NASA/CALIPSO and a global aerosol transport model. *Atmospheric Chemistry and Physics*, *9*(9), 3137–3145. https://doi.org/10.5194/acp-9-3137-2009

Fang, Y., Mauzerall, D. L., Liu, J., Fiore, A. M., & Horowitz, L. W. (2013). Impacts of 21st century climate change on global air pollution-related premature mortality. *Climatic Change*, *121*(2), 239–253. https://doi.org/10.1007/s10584-013-0847-8

Field, P. R., & Wood, R. (2007). Precipitation and cloud structure in midlatitude cyclones. *Journal of Climate*, *20*(2), 233–254. https://doi.org/10.1175/JCLI3998.1

Gelaro, R., McCarty, W., Suárez, M. J., Todling, R., Molod, A., Takacs, L., … Zhao, B. (2017). The Modern-Era Retrospective Analysis for Research and Applications, Version 2 (MERRA-2). *Journal of Climate*, *30*(14), 5419–5454. https://doi.org/10.1175/JCLI-D-16-0758.1

Ginoux, P., Chin, M., Tegen, I., Prospero, J. M., Holben, B., Dubovik, O., & Lin, S.-J. (2001). Sources and distributions of dust aerosols simulated with the GOCART model. *Journal of Geophysical Research: Atmospheres*, *106*(D17), 20255–20273. https://doi.org/10.1029/2000JD000053

Gong, S. L. (2003). A parameterization of sea-salt aerosol source function for sub- and super-micron particles. *Global Biogeochemical Cycles*, *17*(4), 1–7. https://doi.org/10.1029/2003gb002079

Graedel, T. E., & Weschler, C. J. (1981). Chemistry within aqueous atmospheric aerosols and raindrops. In *Reviews of Geophysics* (Vol. 19). https://doi.org/10.1029/RG019i004p00505

Grandey, B. S., Stier, P., Grainger, R. G., & Wagner, T. M. (2013). The contribution of the strength and structure of extratropical cyclones to observed cloud-aerosol relationships. *Atmospheric Chemistry and Physics*, *13*(21), 10689–10701. https://doi.org/10.5194/acp-13-10689-2013

Grandey, B. S., Stier, P., Wagner, T. M., Grainger, R. G., & Hodges, K. I. (2011). The effect of extratropical cyclones on satellite-retrieved aerosol properties over ocean. *Geophysical Research Letters*, *38*(13), 1–6. https://doi.org/10.1029/2011GL047703

Granier, C., Bessagnet, B., Bond, T., D'Angiola, A., van der Gon, H. D., Frost, G. J., … van Vuuren, D. P. (2011). Evolution of anthropogenic and biomass burning emissions of air pollutants at global and regional scales during the 1980-2010 period. *Climatic Change*, *109*(1), 163–190. https://doi.org/10.1007/s10584-011-0154-1

Guibert, S., Matthias, V., Schulz, M., Bösenberg, J., Eixmann, R., Mattis, I., … Vaughan, G. (2005). The vertical distribution of aerosol over Europe - Synthesis of one year of EARLINET aerosol lidar measurements and aerosol transport modeling with LMDzT-INCA. *Atmospheric Environment*, *39*(16), 2933–2943. https://doi.org/10.1016/j.atmosenv.2004.12.046

Hannan, J. R., Fuelberg, H. E., Crawford, J. H., Sachse, G. W., & Blake, D. R. (2003). Role of wave cyclones in transporting boundary layer air to the free troposphere during the spring 2001 NASA/TRACE-P experiment. *Journal of Geophysical Research: Atmospheres*, *108*(20), 1–17. https://doi.org/10.1029/2002jd003105

He, H., Li, C., Loughner, C. P., Li, Z., Krotkov, N. A., Yang, K., … Dickerson, R. R. (2012). SO2 over central China: Measurements, numerical simulations and the tropospheric sulfur budget. *Journal of Geophysical Research Atmospheres*, *117*(3), 1–15. https://doi.org/10.1029/2011JD016473

Hess, M., Koepke, P., & Schult, I. (1998). Optical Properties of Aerosols and Clouds: The Software Package OPAC. *Bulletin of the American Meteorological Society*, *79*(5), 831–844. https://doi.org/10.1175/1520-0477(1998)079<0831:OPOAAC>2.0.CO;2

Hodzic, A., Kasibhatla, P. S., Jo, D. S., Cappa, C. D., Jimenez, J. L., Madronich, S., & Park, R. J. (2016). Rethinking the global secondary organic aerosol (SOA) budget: Stronger production, faster removal, shorter lifetime. *Atmospheric Chemistry and Physics*, *16*(12), 7917–7941. https://doi.org/10.5194/acp-16-7917-2016

Hoskins, B. J., & Hodges, K. I. (2002). New perspectives on the Northern Hemisphere winter storm tracks. *Journal of the Atmospheric Sciences*, *59*(6), 1041–1061. https://doi.org/10.1175/1520-0469(2002)059<1041:NPOTNH>2.0.CO;2

Huang, J., Minnis, P., Chen, B., Huang, Z., Liu, Z., Zhao, Q., … Ayers, J. K. (2008). Long-range transport and vertical structure of Asian dust from CALIPSO and surface measurements during PACDEX. *Journal of Geophysical Research Atmospheres*, *113*(23), 1–13. https://doi.org/10.1029/2008JD010620

Jacobson, M. C., & Hansson, H. (2000). Review Ic Atmosph Eric Aerosols ' Science an D State of the. *Reviews of Geophysics*, (1998), 267–294. https://doi.org/10.1029/1998RG000045

Jaeglé, L., Quinn, P. K., Bates, T. S., Alexander, B., & Lin, J. T. (2011). Global distribution of sea salt aerosols: New constraints from in situ and remote sensing observations. *Atmospheric Chemistry and Physics*, *11*(7), 3137–3157. https://doi.org/10.5194/acp-11-3137-2011

Jaeglé, L., Wood, R., & Wargan, K. (2017). Multiyear Composite View of Ozone Enhancements and Stratosphere-to-Troposphere Transport in Dry Intrusions of Northern Hemisphere Extratropical Cyclones. *Journal of Geophysical Research: Atmospheres*, *122*(24), 13,436-13,457. https://doi.org/10.1002/2017JD027656

Jaffe, D., McKendry, I., Anderson, T., & Price, H. (2003). Six "new" episodes of trans-Pacific transport of air pollutants. *Atmospheric Environment*, *37*(3), 391–404. https://doi.org/10.1016/S1352-2310(02)00862-2

Jickells, T. D., & Spokes, L. J. (2001). Atmospheric iron inputs to the oceans. In *The Biogeochemistry of Iron in Seawater* (pp. 85–121). Wiley.

Joos, H., Madonna, E., Witlox, K., Ferrachat, S., Wernli, H., & Lohmann, U. (2017). Effect of anthropogenic aerosol emissions on precipitation in warm conveyor belts in the western North Pacific in winter - A model study with ECHAM6-HAM. *Atmospheric Chemistry and Physics*, *17*(10), 6243–6255. https://doi.org/10.5194/acp-17-6243-2017

Kerminen, V. M., Lihavainen, H., Komppula, M., Viisanen, Y., & Kulmala, M. (2005). Direct observational evidence linking atmospheric aerosol formation and cloud droplet activation. *Geophysical Research Letters*, *32*(14), 1–4. https://doi.org/10.1029/2005GL023130

Kinne, S., Lohmann, U., Feichter, J., Schulz, M., Timmreck, C., Ghan, S., … Kaufman, Y. (2003). Monthly averages of aerosol properties: A global comparison among models, satellite data, and AERONET ground data. *Journal of Geophysical Research Atmospheres*, *108*(20). https://doi.org/10.1029/2001JD001253

Knowland, K. E., Doherty, R. M., & Hodges, K. I. (2015). The effects of springtime mid-latitude storms on trace gas composition determined from the MACC reanalysis. *Atmospheric Chemistry and Physics*, *15*(6), 3605–3628. https://doi.org/10.5194/acp-15-3605-2015

Larson, E. J. L., & Portmann, R. W. (2019). Anthropogenic aerosol drives uncertainty in future climate mitigation efforts. *Scientific Reports*, *9*(1), 1–8. https://doi.org/10.1038/s41598-019-52901-3

Levy, R. C., Mattoo, S., Munchak, L. A., Remer, L. A., Sayer, A. M., Patadia, F., & Hsu, N. C. (2013). The Collection 6 MODIS aerosol products over land and ocean. *Atmospheric Measurement Techniques*, *6*(11), 2989–3034. https://doi.org/10.5194/amt-6-2989-2013

Levy, Robert C., Remer, L. A., Tanré, D., Kaufman, Y. J., Ichoku, C., Holben, B. N., … Maring, H. (2003). Evaluation of the moderate-resolution imaging spectroradiometer (MODIS) retrievals of dust aerosol over the ocean during PRIDE. *Journal of Geophysical Research: Atmospheres*, *108*(19), 1–13. https://doi.org/10.1029/2002jd002460

Liang, Q., Jaeglé, L., Jaffe, D. A., Weiss-Penzias, P., Heckman, A., & Snow, J. A. (2004). Long-range transport of Asian pollution to the northeast Pacific: Seasonal variations and transport pathways of carbon monoxide. *Journal of Geophysical Research D: Atmospheres*, *109*(23), 1–16. https://doi.org/10.1029/2003JD004402

Luan, Y., & Jaeglé, L. (2013). Composite study of aerosol export events from East Asia and North America. *Atmospheric Chemistry and Physics*, *13*(3), 1221–1242. https://doi.org/10.5194/acp-13-1221-2013

McCarty, W., Coy, L., Gelaro, R., Huang, A., Merkova, D., Smith, E.B., Sienkiewicz, M., Wargan, K. (2016). MERRA-2 input observations: Summary and assessment. *NASA/TM–2016–104606*, *46*, 64.

McCoy, D. T., Field, P. R., Schmidt, A., Grosvenor, D. P., Bender, F. A. M., Shipway, B. J., … Elsaesser, G. S. (2018). Aerosol midlatitude cyclone indirect effects in observations and high-resolution simulations. *Atmospheric Chemistry and Physics*, *18*(8), 5821–5846. https://doi.org/10.5194/acp-18-5821-2018

Molod, A., Takacs, L., Suarez, M., & Bacmeister, J. (2015). Development of the GEOS-5 atmospheric general circulation model: Evolution from MERRA to MERRA2. *Geoscientific Model Development*, *8*(5), 1339–1356. https://doi.org/10.5194/gmd-8-1339-2015

Naud, C. M., Booth, J. F., Jeyaratnam, J., Donner, L. J., Seman, C. J., Zhao, M., … Ming, Y. (2019). Extratropical cyclone clouds in the GFDL climate model: Diagnosing biases and the associated causes. *Journal of Climate*, *32*(20), 6685–6701. https://doi.org/10.1175/JCLI-D-19-0421.1

Naud, C. M., Posselt, D. J., & van den Heever, S. C. (2016). Aerosol optical depth distribution in extratropical cyclones over the Northern Hemisphere oceans. *Geophysical Research Letters*, *43*(19), 10,504-10,511. https://doi.org/10.1002/2016GL070953

Naud, C. M., Posselt, D. J., & van den Heever, S. C. (2017). Observed Covariations of Aerosol Optical Depth and Cloud Cover in Extratropical Cyclones. *Journal of Geophysical Research: Atmospheres*, *122*(19), 10,338-10,356. https://doi.org/10.1002/2017JD027240

Nielsen, J. E., Pawson, S., Molod, A., Auer, B., da Silva, A. M., Douglass, A. R., … Wargan, K. (2017). Chemical Mechanisms and Their Applications in the Goddard Earth Observing System (GEOS) Earth System Model. *Journal of Advances in Modeling Earth Systems*, *9*(8), 3019–3044. https://doi.org/10.1002/2017MS001011

Nowottnick, E., Colarco, P., Ferrare, R., Chen, G., Ismail, S., Anderson, B., & Browell, E. (2010). Online simulations of mineral dust aerosol distributions: Comparisons to namma observations and sensitivity to dust emission parameterization. *Journal of Geophysical Research Atmospheres*, *115*(3), 1–19. https://doi.org/10.1029/2009JD012692

Orbe, C., Oman, L. D., Strahan, S. E., Waugh, D. W., Pawson, S., Takacs, L. L., & Molod, A. M. (2017). Large-Scale Atmospheric Transport in GEOS Replay Simulations. *Journal of Advances in Modeling Earth Systems*, *9*(7), 2545–2560. https://doi.org/10.1002/2017MS001053

Park, R. J., Jacob, D. J., Palmer, P. I., Clarke, A. D., Weber, R. J., Zondlo, M. A., … Bond, T. C. (2005). Export efficiency of black carbon aerosol in continental outflow: Global implications. *Journal of Geophysical Research D: Atmospheres*, *110*(11), 1–7. https://doi.org/10.1029/2004JD005432

Partanen, A. I., Landry, J. S., & Matthews, H. D. (2018). Climate and health implications of future aerosol emission scenarios. *Environmental Research Letters*, *13*(2). https://doi.org/10.1088/1748-9326/aaa511

Patoux, J., Yuan, X., & Li, C. (2009). Satellite-based midlatitude cyclone statistics over the Southern Ocean: 1. Scatterometer-derived pressure fields and storm tracking. *Journal of Geophysical Research*, *114*(D4). https://doi.org/10.1029/2008JD010873

Platnick, S., King, M. D., Meyer, K. G., Wind, G., Amarasinghje, N., Marchant, B., … Riedi, J. (2015). *MODIS Cloud Optical Properties : User Guide for the Collection 6 Level-2 MOD06 / MYD06 Product and Associated Level-3 Datasets*. Retrieved from https://atmosphere-imager.gsfc.nasa.gov/sites/default/files/ModAtmo/C6MOD06OPUserGuide_0.pdf

Prather, K. A., Hatch, C. D., & Grassian, V. H. (2008). Analysis of atmospheric aerosols. *Annual Review of*

Analytical Chemistry, *1*(1), 485–514. https://doi.org/10.1146/annurev.anchem.1.031207.113030

Randles, C. A., da Silva, A. M., Buchard, V., Colarco, P. R., Darmenov, A., Govindaraju, R., … Flynn, C. J. (2017). The MERRA-2 aerosol reanalysis, 1980 onward. Part I: System description and data assimilation evaluation. *Journal of Climate*, *30*(17), 6823–6850. https://doi.org/10.1175/JCLI-D-16-0609.1

Real, E., Pisso, I., Law, K. S., Legras, B., Bousserez, N., Schlager, H., … Attié, J. L. (2010). Toward a novel high-resolution modeling approach for the study of chemical evolution of pollutant plumes during long-range transport. *Journal of Geophysical Research Atmospheres*, *115*(12), 1–14. https://doi.org/10.1029/2009JD011707

Remer, A, L., Kaufman, Y. J., Tanré, D., Mattoo, S., Chu, D. A., … and B N Holben. (2005). The MODIS Aerosol Algorithm, Products, and Validation. *Journal of the Atmospheric Sciences*, *62*(4), 947–973.

Remer, L. A., Kleidman, R. G., Levy, R. C., Kaufman, Y. J., Tanré, D., Mattoo, S., … Holben, B. N. (2008). Global aerosol climatology from the MODIS satellite sensors. *Journal of Geophysical Research Atmospheres*, *113*(14), 1–18. https://doi.org/10.1029/2007JD009661

Shindell, D. T., Lamarque, J. F., Schulz, M., Flanner, M., Jiao, C., Chin, M., … Lo, F. (2013). Radiative forcing in the ACCMIP historical and future climate simulations. *Atmospheric Chemistry and Physics*, *13*(6), 2939–2974. https://doi.org/10.5194/acp-13-2939-2013

Silva, R. A., West, J. J., Lamarque, J. F., Shindell, D. T., Collins, W. J., Faluvegi, G., … Zeng, G. (2017). Future global mortality from changes in air pollution attributable to climate change. *Nature Climate Change*, *7*(9), 647–651. https://doi.org/10.1038/nclimate3354

Simpson, I. R., Shaw, T. A., & Seager, R. (2014). A diagnosis of the seasonally and longitudinally varying midlatitude circulation response to global warming. *Journal of the Atmospheric Sciences*, *71*(7), 2489–2515. https://doi.org/10.1175/JAS-D-13-0325.1

Sinclair, V. A., Gray, S. L., & Belcher, S. E. (2008). Boundary-layer ventilation by baroclinic life cycles. *Quarterly Journal of the Royal Meteorological Society*, *134*(635), 1409–1424. https://doi.org/10.1002/qj.293

Smith, S. J., & Bond, T. C. (2014). Two hundred fifty years of aerosols and climate: The end of the age of aerosols. *Atmospheric Chemistry and Physics*, *14*(2), 537–549. https://doi.org/10.5194/acp-14-537-2014

Stohl, A. (2001). A 1-year Lagrangian “climatology” of airstreams in the Northern Hemisphere troposphere and lowermost stratosphere. *Journal of Geophysical Research Atmospheres*, *106*(D7), 7263–7279. https://doi.org/10.1029/2000JD900570

Strahan, S. E., Duncan, B. N., & Hoor, P. (2007). Observationally derived transport diagnostics for the lowermost stratosphere and their application to the GMI chemistry and transport model. *Atmospheric Chemistry and Physics*, *7*(9), 2435–2445. https://doi.org/10.5194/acp-7-2435-2007

Strode, S. A., Ziemke, J. R., Oman, L. D., Lamsal, L. N., Olsen, M. A., & Liu, J. (2019). Global changes in the diurnal cycle of surface ozone. *Atmospheric Environment*, *199*(August 2018), 323–333. https://doi.org/10.1016/j.atmosenv.2018.11.028

Szopa, S., V. Naik, B. Adhikary, P. Artaxo, T. Berntsen, W.D. Collins, S. Fuzzi, L. Gallardo, A. Kiendler-Scharr, Z. Klimont, H. Liao, N. Unger, and P. Zanis, 2021: Short-Lived Climate Forcers. In Climate Change 2021: The Physical Science Basis. *Contribution of Working Group I to the Sixth Assessment Report of the Intergovernmental Panel on Climate Change* [Masson-Delmotte, V., P. Zhai, A. Pirani, S.L. Connors, C. Péan, S. Berger, N. Caud, Y. Chen, L. Goldfarb, M.I. Gomis, M. Huang, K. Leitzell, E. Lonnoy, J.B.R. Matthews, T.K. Maycock, T. Waterfield, O. Yelekçi, R. Yu, and B. Zhou (eds.)]. Cambridge University Press, Cambridge, United Kingdom and New York, NY, USA, pp. 817–922, doi:10.1017/9781009157896.008

Turnock, S. T., Allen, R. J., Andrews, M., Bauer, S. E., Deushi, M., Emmons, L., … Zhang, J. (2020). Historical and future changes in air pollutants from CMIP6 models. *Atmospheric Chemistry and Physics*, *20*(23), 14547–14579. https://doi.org/10.5194/acp-20-14547-2020

Ulbrich, U., Leckebusch, G. C., & Pinto, J. G. (2009). *Extra-tropical cyclones in the present and future climate : a review*. 117–131. https://doi.org/10.1007/s00704-008-0083-8

Wang, Y., Zhang, R., & Saravanan, R. (2014). Asian pollution climatically modulates mid-latitude cyclones following hierarchical modelling and observational analysis. *Nature Communications*, *5*. https://doi.org/10.1038/ncomms4098

Wei, J., Li, Z., Peng, Y., & Sun, L. (2019a). MODIS Collection 6.1 aerosol optical depth products over land and ocean: validation and comparison. *Atmospheric Environment*, *201*(October 2018), 428–440. https://doi.org/10.1016/j.atmosenv.2018.12.004

Wei, J., Peng, Y., Guo, J., & Sun, L. (2019b). Performance of MODIS Collection 6.1 Level 3 aerosol products in spatial-temporal variations over land. *Atmospheric Environment*, *206*(September 2018), 30–44. https://doi.org/10.1016/j.atmosenv.2019.03.001

Weng, H., Lin, J., Martin, R., Millet, D. B., Jaeglé, L., Ridley, D., … Meng, J. (2020). Global high-resolution emissions of soil NOx, sea salt aerosols, and biogenic volatile organic compounds. *Scientific Data*, *7*(1), 1–15. https://doi.org/10.1038/s41597-020-0488-5

Wernli, H., & Schwierz, C. (2006). Surface cyclones in the ERA-40 dataset (1958-2001). Part I: Novel identification method and global climatology. *Journal of the Atmospheric Sciences*, *63*(10), 2486–2507. https://doi.org/10.1175/JAS3766.1

Westervelt, D. M., Horowitz, L. W., Naik, V., Golaz, J. C., & Mauzerall, D. L. (2015). Radiative forcing and climate response to projected 21st century aerosol decreases. *Atmospheric Chemistry and Physics*, *15*(22), 12681–12703. https://doi.org/10.5194/acp-15-12681-2015

Whitaker, J. S., Uccellini, L. W., & Brill, K. F. (1988). A Model-Based Diagnostic Study of the Rapid Development Phase of the Presidents's Day Cyclone. *Monthly Weather Review*, *116*(11), 2337–2365. https://doi.org/10.1175/1520-0493(1988)116<2337:AMBDSO>2.0.CO;2

Yang, Q., Easter, R. C., Campuzano-Jost, P., Jimenez, J. L., Fast, J. D., Ghan, S. J., … Wisthaler, A. (2015). Aerosol transport and wet scavenging in deep convective clouds: A case study and model evaluation using a multiple passive tracer analysis approach. *Journal of Geophysical Research: Atmospheres*, *120*(16), 8448–8468. https://doi.org/10.1002/2015JD023647

Yang, Y., Liao, H., & Lou, S. (2015). Decadal trend and interannual variation of outflow of aerosols from East Asia: Roles of variations in meteorological parameters and emissions. *Atmospheric Environment*, *100*, 141–153. https://doi.org/10.1016/j.atmosenv.2014.11.004

Yu, H., Remer, L. A., Chin, M., Bian, H., Kleidman, R. G., & Diehl, T. (2008). A satellite-based assessment of transpacific transport of pollution aerosol. *Journal of Geophysical Research*, *113*(D14), 1–15. https://doi.org/10.1029/2007jd009349

Zhang, R., Li, G., Fan, J., Wu, D. L., & Molina, M. J. (2007). Intensification of Pacific storm track linked to Asian pollution. *Proceedings of the National Academy of Sciences of the United States of America*, *104*(13), 5295–5299. https://doi.org/10.1073/pnas.0700618104

AGU PUBLICATIONS

Journal of Geophysical Research: Atmospheres

Supporting Information for

The Role of Midlatitude Cyclones in the Emission, Transport, Production, and Removal of Aerosols in the Northern Hemisphere

Joseph Robinson[1], Lyatt Jaeglé[1], Luke D. Oman[2]

[1]Department of Atmospheric Sciences, University of Washington, Seattle, WA, USA

[2]Atmospheric Chemistry and Dynamics Laboratory, NASA Goddard Space Flight Center, Greenbelt, MD, USA

Contents of this file

Text S1.

The equation below describes the relationship between aerosol extinction (*Ext*), dry mass (M_d), and extinction efficiency (β). To first order, enhancements in extinction (ΔExt) are equal to the sum of enhancements in dry aerosol mass (ΔM_d) and mass extinction efficiency ($\Delta\beta$). Starting with the definition of extinction:

$$Ext = \beta \times M_d$$

Expressing ΔExt relative to background conditions, where prime denotes background, then simplifying:

$$\Delta Ext = \frac{Ext - Ext'}{Ext'} = \frac{Ext}{Ext'} - 1 = \frac{\beta \times M_d}{\beta' \times M_d'} - 1 = \frac{M_d}{\frac{M_d{}' \times \beta}{\beta'}} - 1 =$$
$$(\Delta M_d + 1)(\Delta\beta + 1) - 1 = \Delta M_d \Delta\beta + \Delta M_d + \Delta\beta$$

Neglecting the term of order two, $\Delta M_d \Delta\beta$, yields:

$$\Delta Ext \approx \Delta M_d + \Delta\beta$$

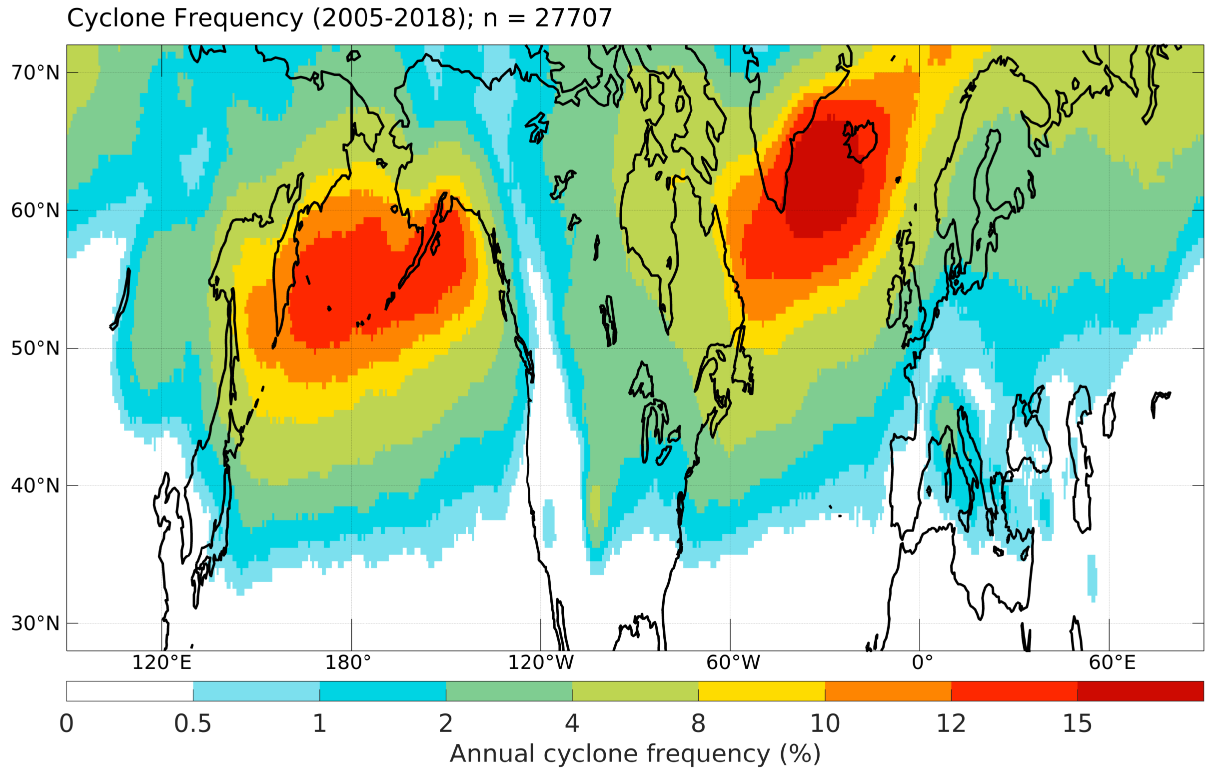

Figure S1. Annual mean NH midlatitude cyclone occurrence frequency for 2005-2018.

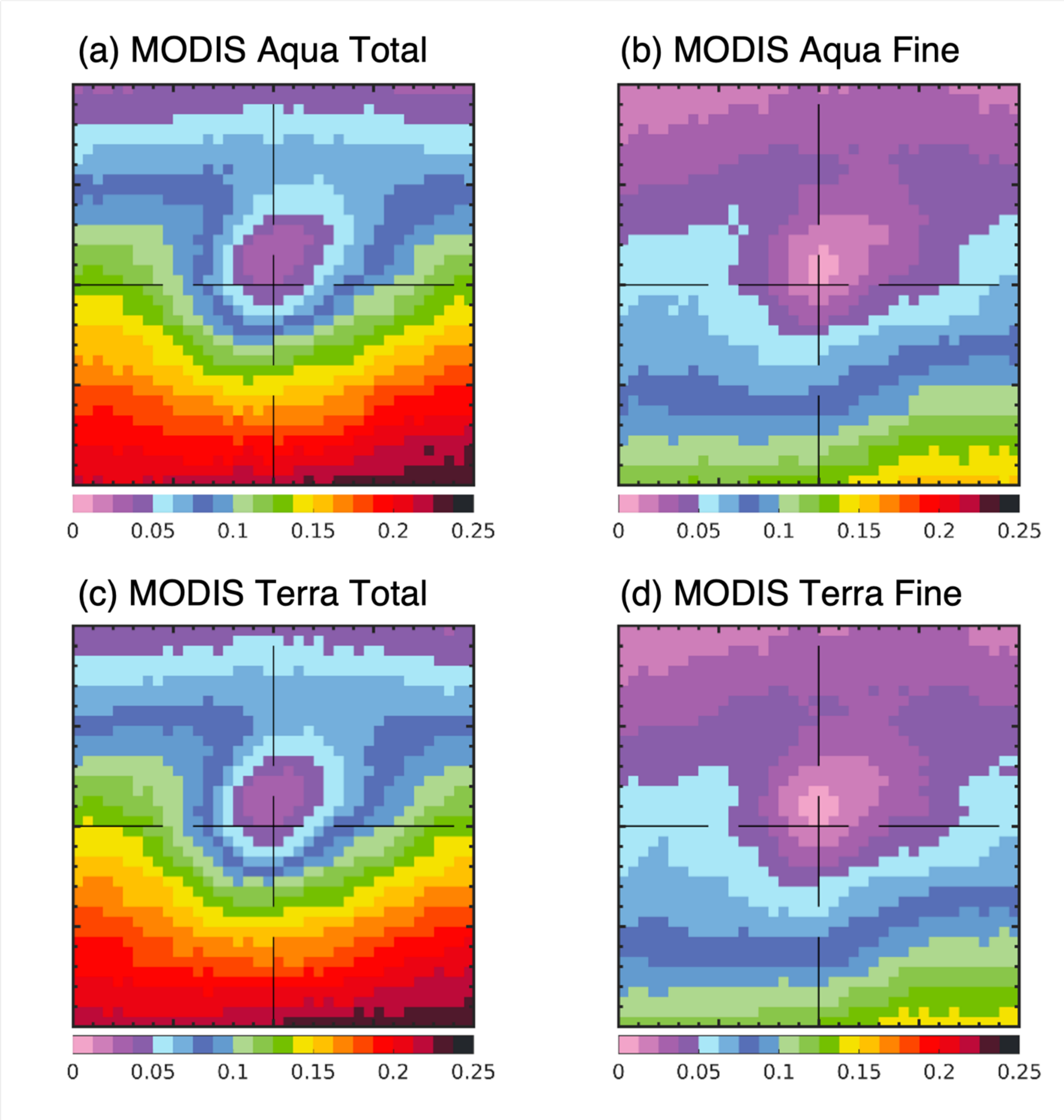

Figure S2. The fraction of 27,707 northern hemisphere midlatitude cyclones with valid data in the MODIS observations. (a) Fraction of cyclones with valid data for MODIS Aqua total AOD. (b) Same as (a) but for MODIS Aqua fine/coarse AOD. (c) Same as (a) but for MODIS Terra total AOD. (d) Same as (a) but for MODIS Terra fine/coarse AOD.

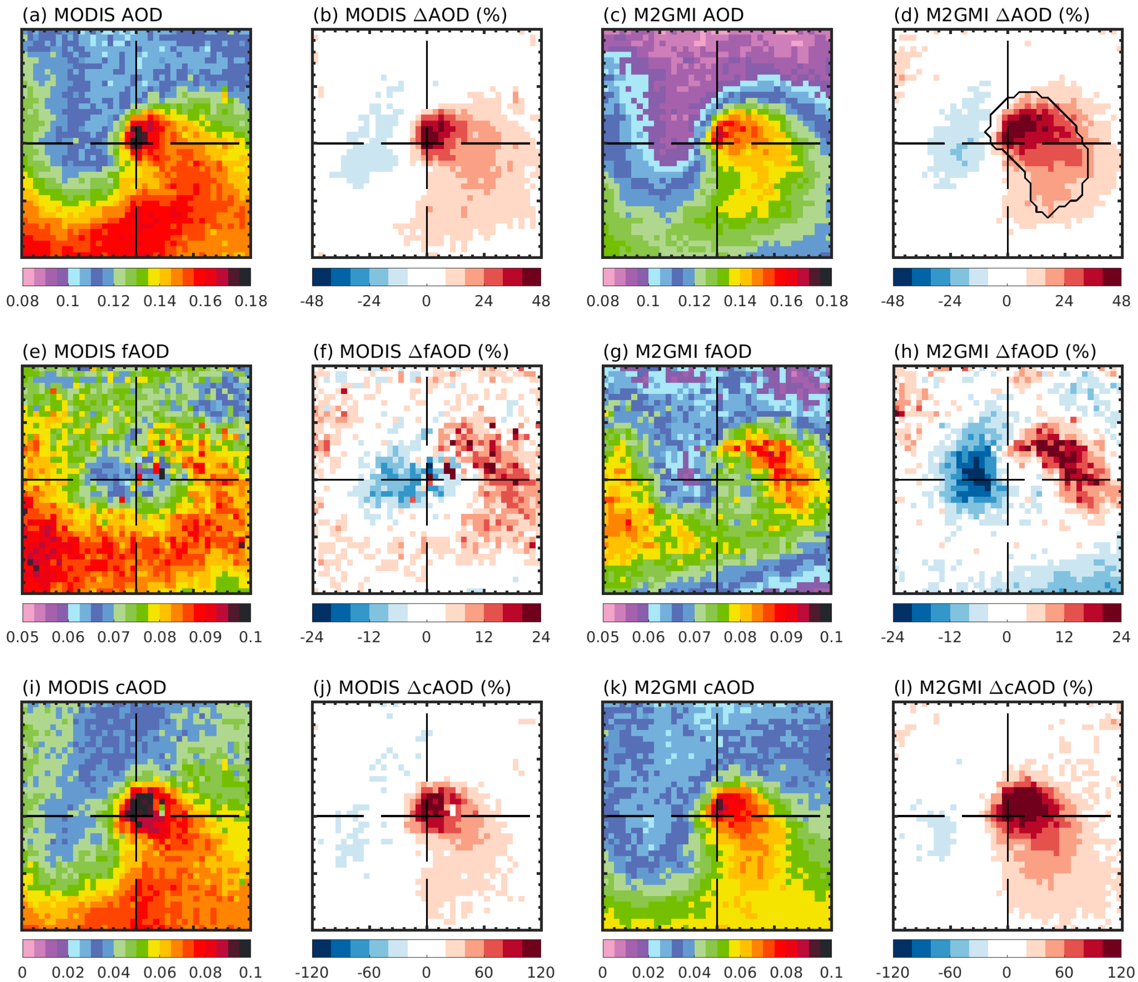

Figure S3. Same as Figure 2 of the main text but for MODIS Terra and the M2GMI model sampled at the Terra overpass time.

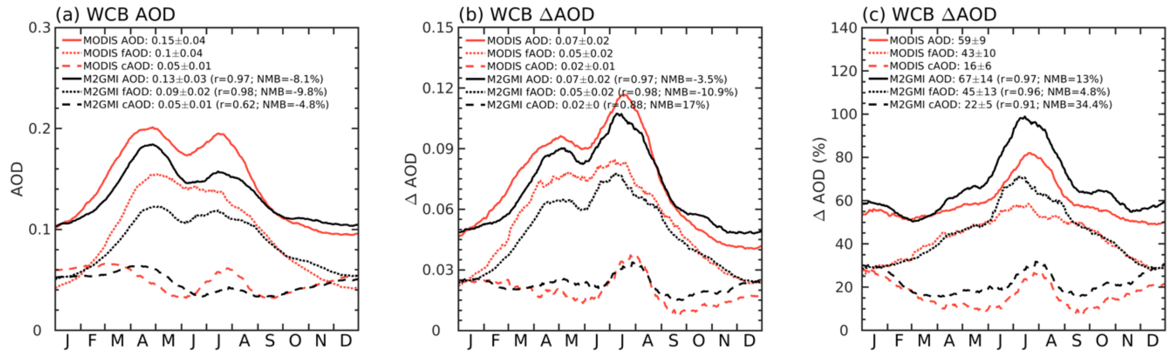

Figure S4. Same as Figure 3 of the main text but for MODIS Terra and the M2GMI model sampled at the Terra overpass time.

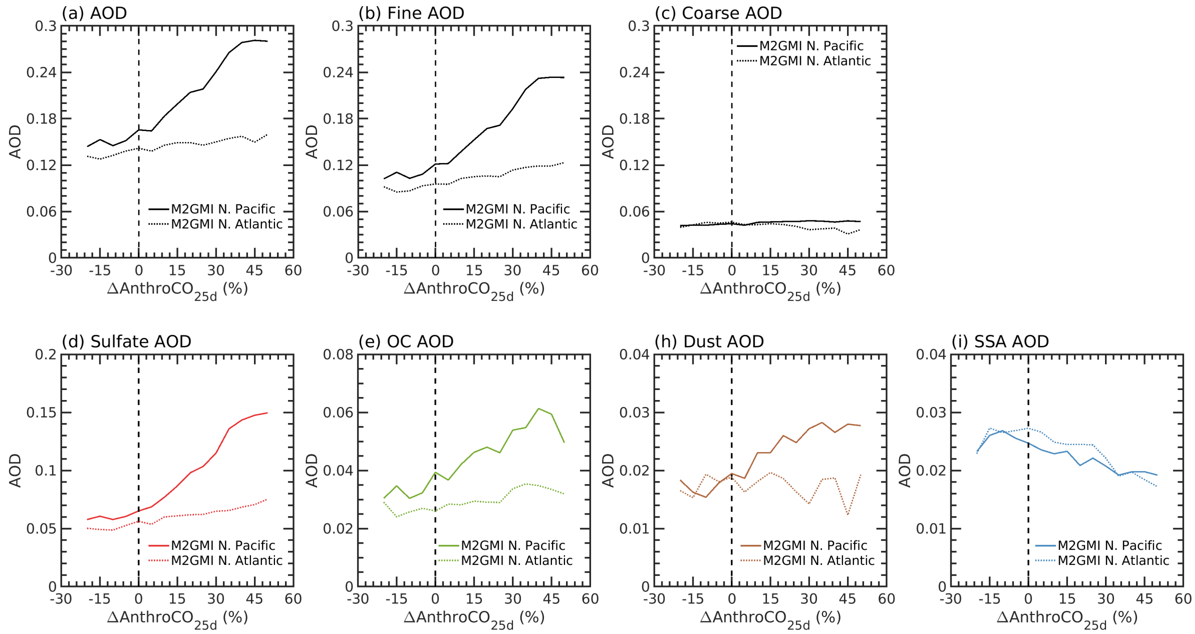

Figure S5. (a-c) Same as Figure 6 in the main text but for the full, daily-averaged M2GMI simulation. (d) Same as (a) but for sulfate AOD. (e) Same as (a) but for organic carbon AOD. (f) same as (a) but for dust AOD. (g) same as (a) but for sea salt AOD.

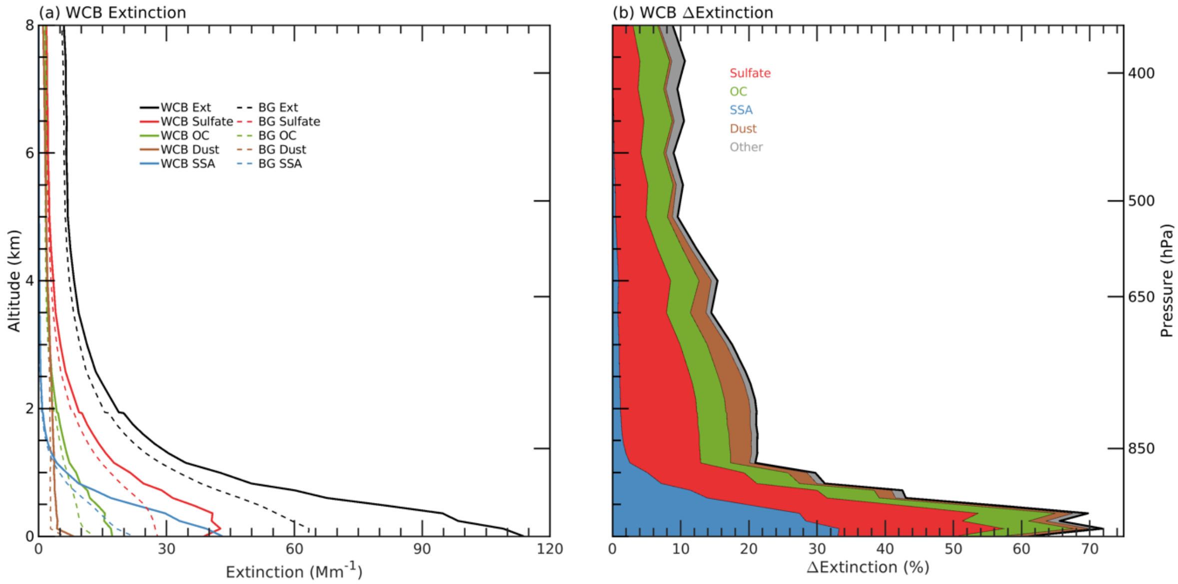

Figure S6. Annual mean vertical profiles of M2GMI aerosol extinction (units of Mm^{-1}) in the WCB of midlatitude cyclones. (a) Absolute extinction values (solid lines), and background extinction values (dashed lines). Resulting column AOD values for the cyclone profiles are given in the legend. (b) Extinction enhancement given as a percent relative to the total background. The individual component (colored) lines add together to the total extinction enhancement (black line).

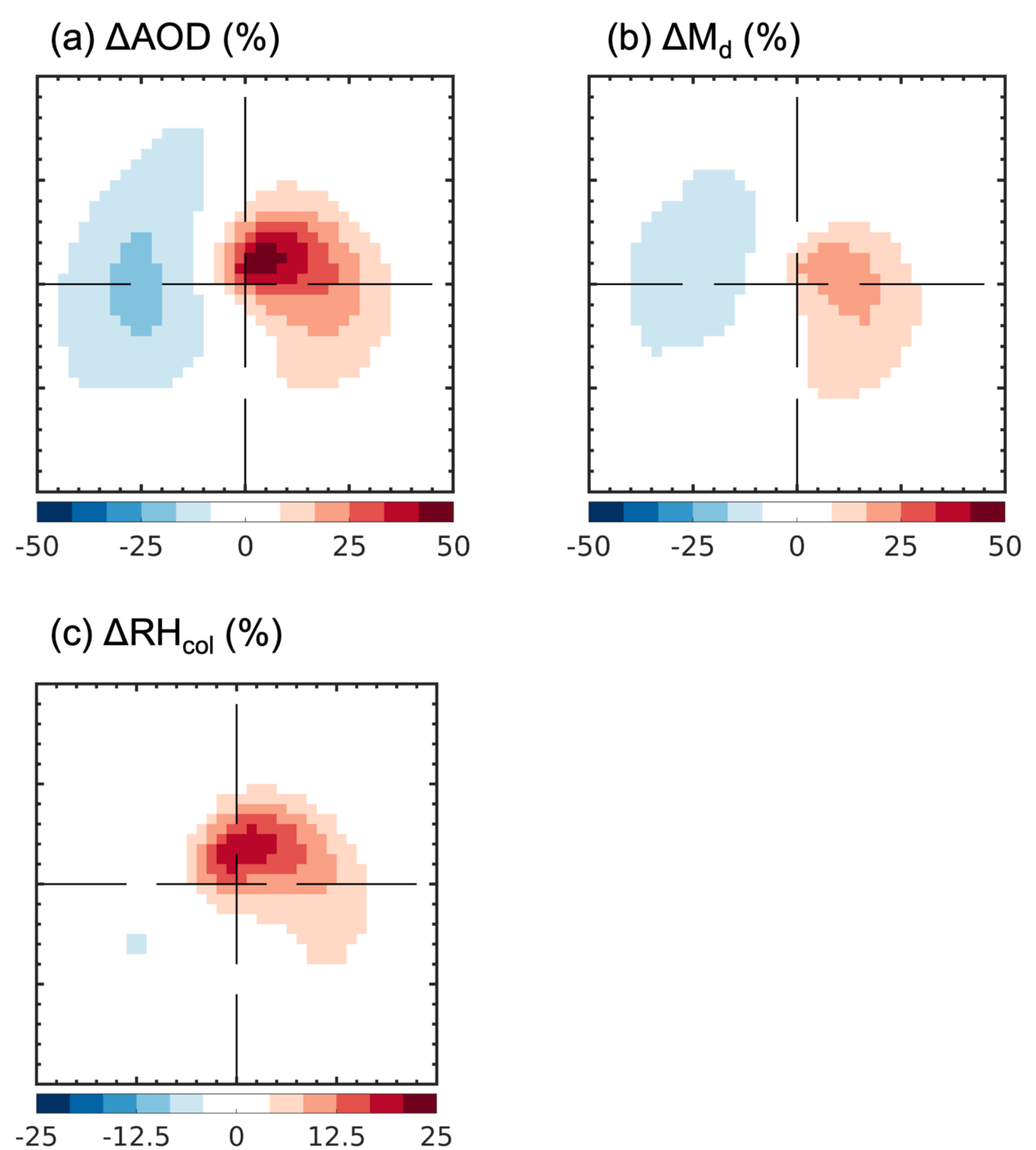

Figure S7. Annual mean composites of 27,707 midlatitude cyclones from M2GMI (2005-2018). (a) Total AOD anomaly (%; same as Figure 5f of the main text). (b) Total dry mass anomaly (%). Each aerosol component's dry mass has been weighted by its contribution to the background AOD (section 5 of the main text). (c) Column average relative humidity anomaly (%).

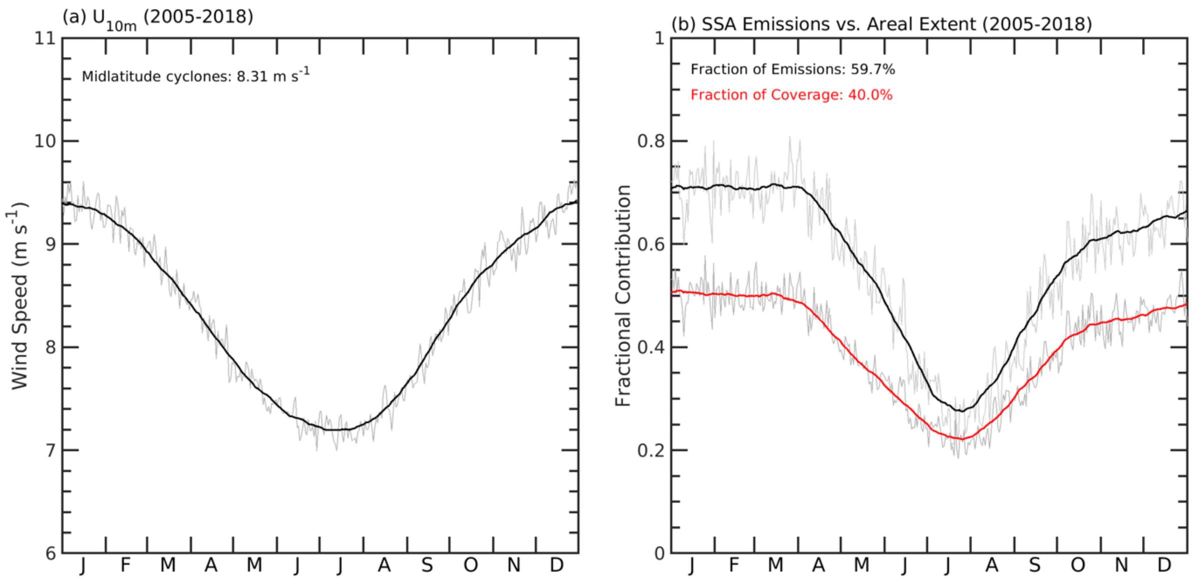

Figure S8. (a) Annual cycle of NH midlatitude cyclone 10 m wind speed (daily values are in gray while the black line shows wind speeds smoothed with a 40-day boxcar average). (b) Annual cycle of fraction of sea salt aerosol emissions due to midlatitude cyclones (daily values in gray with the black line showing the contribution smoothed with a 40-day boxcar average). Also shown is the fraction of NH ocean area covered by the strong wind speed regions of midlatitude cyclones (daily values in gray with the red line showing the area coverage smoothed with a 40-day boxcar average).